Letter of Intent

A Physics Program Based on a New Asymmetrical Electron-Positron Collider for the regime $1.4 < \sqrt{s} < 2.5$ GeV

V.Blinov, , S.I.Eidelman, V.Golubev, B.Khazin, V.N.Ivanchenko, E.Onuchin, S.I.Serednyakov, E.P.Solodov

Budker Institute of Nuclear Physics, Novosibirsk 630090, Russia

M.Mandelkern, C.Munger, J.Schultz

University of California at Irvine, Irvine, CA 92697, USA

M. Placidi

CERN, 1211 Genève 23, Switzerland

W.Baldini, D.Bettoni, R.Calabrese, G.Ciullo, P.Dalpiaz, P.F.Dalpiaz, P.Lenisa, E.Luppi, M.Martini, M.Negrini, F.Petrucci, M.Savrié

INFN and University of Ferrara, 44100 Ferrara, Italy

R.Baldini, S.Bellucci, M.Bertani, M. Ferrer, P.LeviSandri, P.Patteri, A.Zallo

INFN Laboratori Nazionali di Frascati, 00044 Frascati, Italy

M.Schioppa

INFN Gr.Coll. di Frascati and University of Calabria, Arcavacata di Rende, 87036 Cosenza, Italy

U. Mallik

The University of Iowa, Iowa City, IA 52242, USA

R.Arnold, P.Bosted, G.Peterson, S.Rock

University of Massachussets, Amherst, MA 01003, USA

D.Piccolo

INFN and University of Napoli, 80126 Napoli, Italy

M.Morandin, M.Posocco, P.Sartori, R. Stroili, C. Voci

INFN and University of Padova, 35131 Padova, Italy

C.Bini, P.Gauzzi, E.Pasqualucci

INFN and University of Roma 'La Sapienza', 00185 Roma, Italy

V.Bidoli, R.Messi, L.Paoluzi

INFN and University of Roma 'Tor Vergata', 00133 Roma, Italy

P.Paolucci

SLAC, P.O. Box 4349, Stanford, CA 94309, USA

S.Conetti, D.B.Day, B.E.Norum

University of Virginia, Charlottesville, VA 22901, USA

I. ABSTRACT

We propose a comprehensive physics program at an asymmetrical collider consisting of the PEP-II LER and a new electron storage ring (VLER) of energy 140 MeV $< E_e <$ 500 MeV, to be constructed in the IR-12 hall at PEP-II. The accessible center of mass energies will then be 1.4 GeV $< \sqrt{s} <$ 2.5 GeV. This is an energy regime that is inadequately explored in electron-positron annihilations. While accessible to the first generation of (low integrated luminosity) colliders (ADONE, DCI), it is between the upper reach of VEPP-2M and DAϕNE and the lower reach of SPEAR and BEPC. We anticipate approximately 5 years of data taking at an instantaneous luminosity of $\sim 0.5 \times 10^{31}$ cm^{-2} s^{-1}, depending on the VLER energy, for an integrated luminosity in excess of $\sim$ 200 pb^{-1} (in a parasitic mode while BaBar is running). The latter compares favorably with the 10 pb^{-1} collected by experiments at the DCI and VEPP-2M colliders and, in the case of $e^+e^- \to n\overline{n}$, with about 1 pb^{-1} collected by one experiment only.

While there are many important physics measurements that are feasible at this collider, a lot of emphasis will be on R, the ratio of the hadron and muon pair cross sections, and on the determination of nucleon, hyperon and meson timelike form factors.

R is poorly measured in this region. A high precision measurement of R at finely spaced energy intervals is required to accurately evolve the electromagnetic coupling constant in the low energy regime ($\alpha_{EM}(0)$) to the Z scale ($\alpha_{EM}(M_Z^2)$). The latter value is required for prediction of the Higgs mass. Similar hadronic corrections are required for the accurate calculations needed for precision tests of the Standard Model such as the new BNL $g_\mu - 2$ experi-

ment. The proposed new data would reduce the Standard Model uncertainty to a level below the expected statistical error on $g_\mu - 2$, greatly improving the discovery potential of this and similar experiments.

Better nucleon electromagnetic form factor data will hopefully resolve many puzzles posed by the (poor) existing data, in particular by the neutron timelike form factor measurement, which is several times larger than expected. Precise data will confront QCD in the interesting region between the non-perturbative and perturbative regimes. The new measurements will have much smaller statistical errors than previous experiments and will for the first time allow clear separation of the electric and magnetic form factors of the nucleons. We anticipate making the first measurements of timelike nucleon-nucleon resonance transition form factors. Of the hyperon form factors, only that of the Λ is (badly) measured and measurements of the Λ, charged and neutral Σ and $\Lambda - \Sigma$ form factors will provide motivation for theoretical advances in baryon structure.

Pion and charged and neutral kaon timelike electromagnetic form factors are poorly measured above $Q^2 \sim 2$ GeV^2. Vector meson form factors are essentially unmeasured. Both pseudoscalar and vector meson form factors represent potentially tractable applications of perturbative QCD and high precision measurements will complement the active ongoing theoretical efforts in this field.

Electron-positron annihilations are ideal for detecting 1^{--} states, of which eight have been reported in this region, but with poor determinations of branching ratios, masses and widths.

Exclusive multi-hadron final states will also be measured to search for exotic and non-exotic resonances in production, such as those recently reported in antiproton annihilation experiments at LEAR and in diffractive photoproduction at FNAL.

Table of Contents

- APPENDIX I : Nucleon timelike form factors.
- APPENDIX II: Meson timelike form factors.
- APPENDIX III: Form factors via initial state radiation at BaBar.
- APPENDIX IV: University of Virginia Neutron Detector.

II. SCOPE OF THE PROJECT

There is a rich variety of important measurements that are accessible to an electron-positron collider in the center of mass energy range $1.4 < \sqrt{s} < 2.5$ GeV. Many of these are described below. The variety of required running conditions and detector features is such that it may not be possible to do all of the important physics with a single integrated detector. For example the cross sections, energy interval of interest, detector and acceptance requirements for determination of the timelike neutron form factors are very different from those required for an accurate measurement of R, the ratio of hadronic to pointlike cross sections.

Therefore we envision what is effectively a program rather than a single experiment and anticipate that different experimental configurations and running conditions will be established in different data-taking cycles in order to achieve the physics goals set forward below. We expect the active period of data taking to last for approximately five years. Driven by practical considerations, one can imagine that the initial experimental configuration will be relatively simple, followed by a gradual increase in the complexity of the detector systems and well as an increase in the machine luminosity and possibly the useful energy range for collisions.

III. PHYSICS MOTIVATION

A. The importance of R

Testing the consistency of the standard model requires a wide variety of measurements for which the radiative corrections often play a critical role. One such correction, the hadronic vacuum polarization diagram shown in Fig. 1, contributes significantly to $g_\mu - 2$ and the evolution of α_{EM}. The value of $\alpha_{EM}(M_Z^2)$ is vital for determining the mass of the Higgs. The vacuum polarization diagram can be determined directly from the ratio $R = \sigma(e^+ + e^- \to \text{hadrons})/\sigma(e^+ + e^- \to \mu^+ + \mu^-)$. We propose to obtain an accuracy on R of 2.5% in the range $1.4 < \sqrt{s} < 2.5$ GeV, which would significantly reduce the uncertainty of the calculated value of the mass of the Higgs and reduce the errors on the calculated value of $g_\mu - 2$ to below the experimental errors.

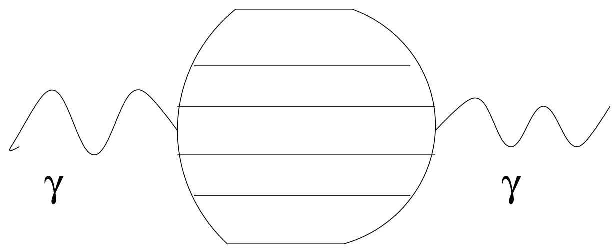

FIG. 1. The Feynman diagram that contributes to the hadronic part of $g_\mu - 2$ and the evolution of α_{EM}.

1. α_{EM}

The value of the QED coupling at the Z pole, $\alpha_{EM}(M_Z^2)$, is the most poorly determined of the three parameters $(G_F, M_Z, \alpha_{EM}(M_Z^2))$ that define the standard electroweak model. Indeed it is the precision to which we know $\alpha_{EM}(M_Z^2)$ that limits the accuracy of the indirect prediction of the mass M_H of the (standard model) Higgs boson [1].

The evolution of α_{EM} is given by:

$$\alpha_{EM}(s)^{-1} = [1 - \Delta\alpha_{lep}(s) - \Delta\alpha^5_{had}(s) - \Delta\alpha^{top}(s)]\alpha^{-1}_{EM}(0). \tag{1}$$

The hadronic term can be calculated using:

$$\Delta\alpha^5_{had}(s) = -\frac{\alpha_{EM}(0)s}{3\pi} P \int_{4m_\pi^2}^{\infty} \frac{R(s\prime)ds'}{s'(s'-s)} \tag{2}$$

where R=$\sigma(e^+ + e^- \rightarrow \text{hadrons})/\sigma(e^+ + e^- \rightarrow \mu^+ + \mu^-)$, $\alpha^{-1}_{EM}(0) = 137.0359895(61)$ and P denotes principal value. The integral is weighted toward the low energy contributions due to the $1/s'$ in the integrand. There have been many efforts to calculate $\Delta\alpha^5_{had}(M_Z^2)$ [1–6] from experimental data supplemented by theoretical models such as PQCD at high energy, non-perturbative gluon and light quark condensates, analyticity, space-like calculations etc.

Not only do the calculated values range from 0.02804 [2] to 0.02763 [3], but there is a wide range of errors, from 0.00065 [2] to 0.00016 [3]. Fortunately, new data have been published from CND-2 [9] and SND [10] at VEPP-2M at $\sqrt{s} < 1.4$ GeV and BES [11] at $\sqrt{s} > 2.5$ GeV and preliminary BES-II data [12] for 2 GeV $< \sqrt{s} <$ 3 GeV. The release of the new BES-II data has led to new calculations within the last month by by Pietrzyk [7] (experiment only: $\Delta\alpha^5_{had}(M_Z^2) = .02755 \pm .00046$) and Martin [8] (with 2 different model dependence: 0.02742 ± 0.00025 and 0.02770 ± 0.00029).

Unfortunately, the critical energy range $1.4 < \sqrt{s} < 2.0$ GeV still suffers from old data of limited precision and is out of the range of existing colliders. Fig. 2 taken from ref. [13] shows the large experimental errors and possible structure in this energy region. Different theoretical modeling of the data in this region (inclusive data compared to exclusive data) [8] yield $\Delta\alpha^5_{had}(M_Z^2) = 0.02742 \pm 0.00025$ and 0.02770 ± 0.0029 respectively. This uncertainty introduces error into the prediction of the Higgs Mass M_H in Standard Model calculations. Using an analytic approximation [2] we find that at $M_H \sim 100$ GeV, $\delta M_H(\text{GeV}) \sim -32000\delta\Delta\alpha^5_{had}(M_Z^2)$. Thus the current experimental error [7] of $\delta\Delta\alpha^5_{had}(M_Z^2) = \pm 0.00046$ corresponds to $\delta M_H = \pm 15$ GeV. This uncertainty is consistent with the results of the LEP Electroweak Working group [14], which determined an error of 0.2 on $\log M_H(\text{GeV})$ due to $\delta\Delta\alpha^5_{had}(M_Z^2) = 0.00065$. This is illustrated in Fig. 3 taken from [7] where the two curves with the lowest value of M_H correspond to $\Delta\alpha^5_{had}(M_Z^2) = 0.02804$ (M_H =62 GeV) and a change of $\Delta\alpha^5_{had}(M_Z^2)$ by .00065 (changing α^{-1}_{EM} by 0.09) corresponding to $\delta M_H \sim 30$ GeV. With the direct search limits on M_H now being well over 100 GeV, the consistency of the standard model depends critically on the value of $\Delta\alpha^5_{had}(M_Z^2)$.

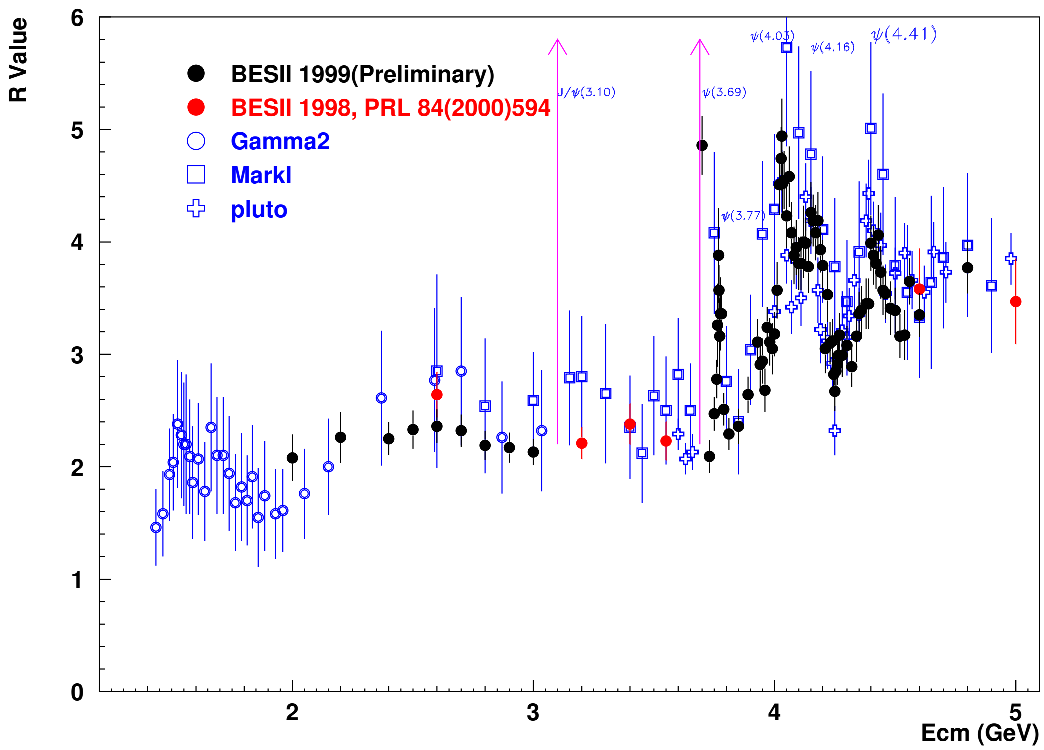

FIG. 2. R vs. center of mass energy in the low energy regime. The solid circles are the new preliminary results from BES-II [12]. The region below 2 GeV still has large errors and may have structure. The figure is taken from ref. [13].

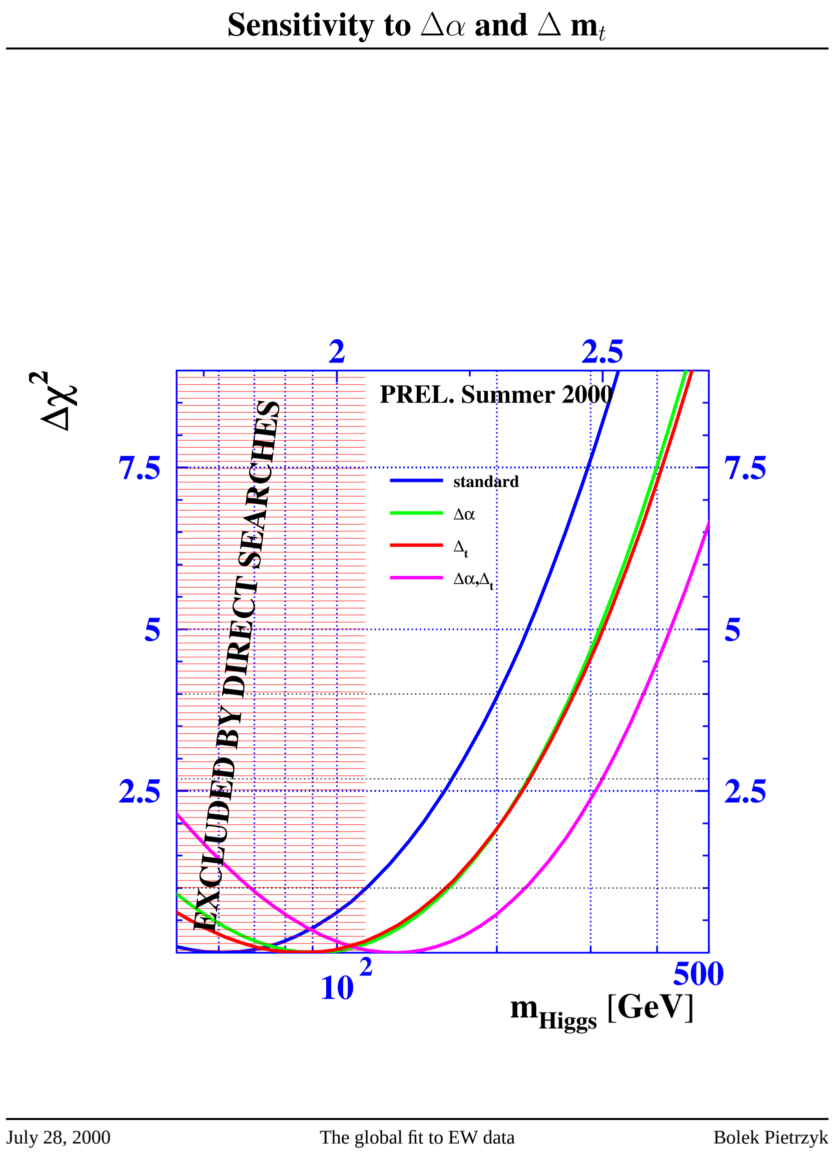

FIG. 3. The effect of changing α_{EM}^{-1} by 0.09 ($\delta\Delta\alpha^5_{had}(M_Z^2) = .00065$) as calculated by Pietrzyk [7] on the mass of the Higgs. The three curves with increasing Higgs mass correspond to $\Delta\alpha^5_{had}(M_Z^2) = 0.02804$, increasing α_{EM}^{-1} by 0.09, and changing both $\Delta\alpha^5_{had}(M_Z^2)$ by 0.09 and M_t by 5.1 GeV.

The effect of $\delta\Delta\alpha^5_{had}(M_Z^2)$ on the electroweak calculations is illustrated in Fig. 4. There is a corresponding uncertainty in $\sin^2\theta_{eff}^{lept}$ of 0.00023 (see Figure 5).

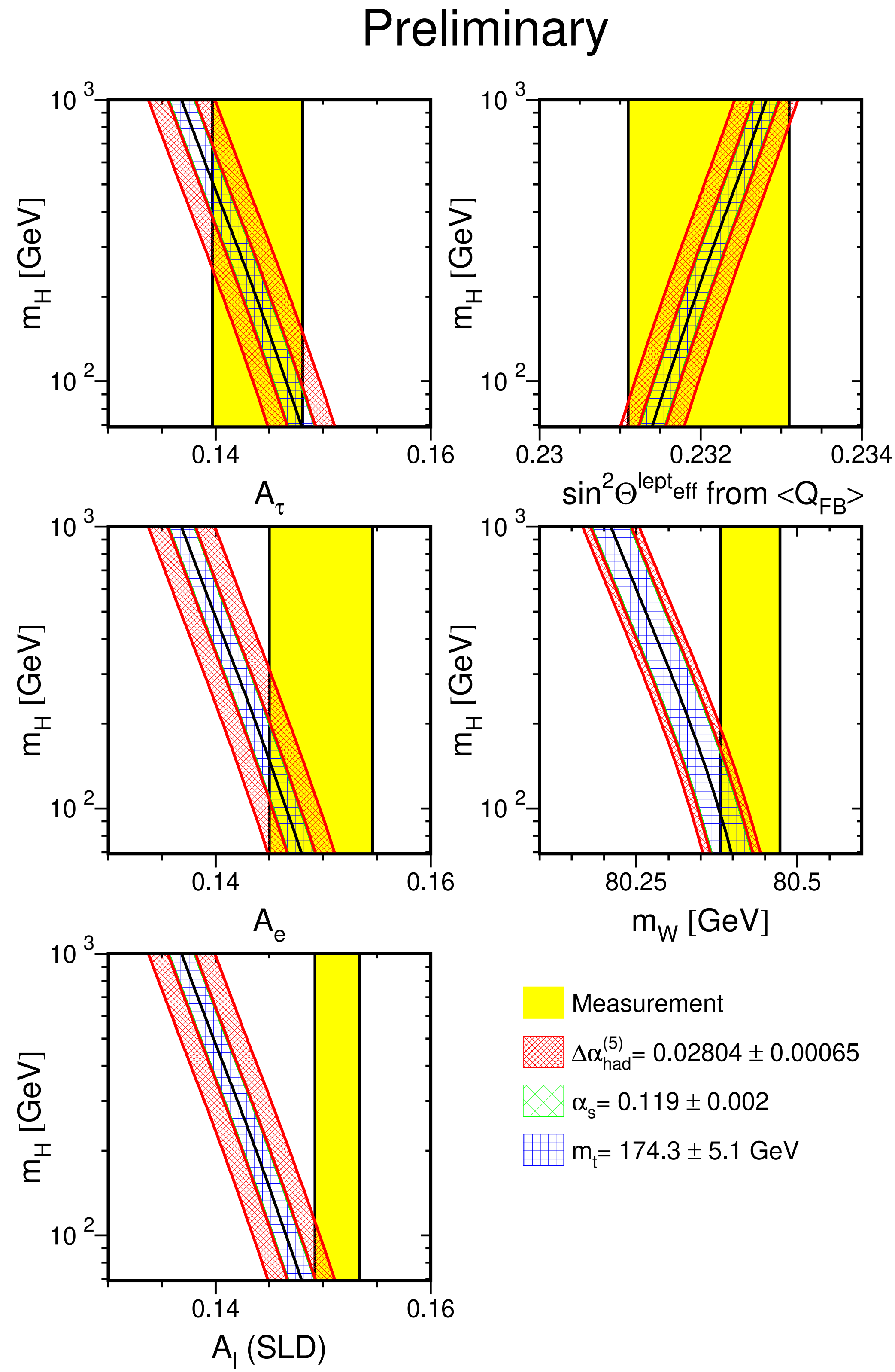

FIG. 4. The effect of the errors in $\Delta\alpha^5_{had}(M_Z^2)$ on the determination of the M_H as calculated by the LEP Electroweak Working group [14].

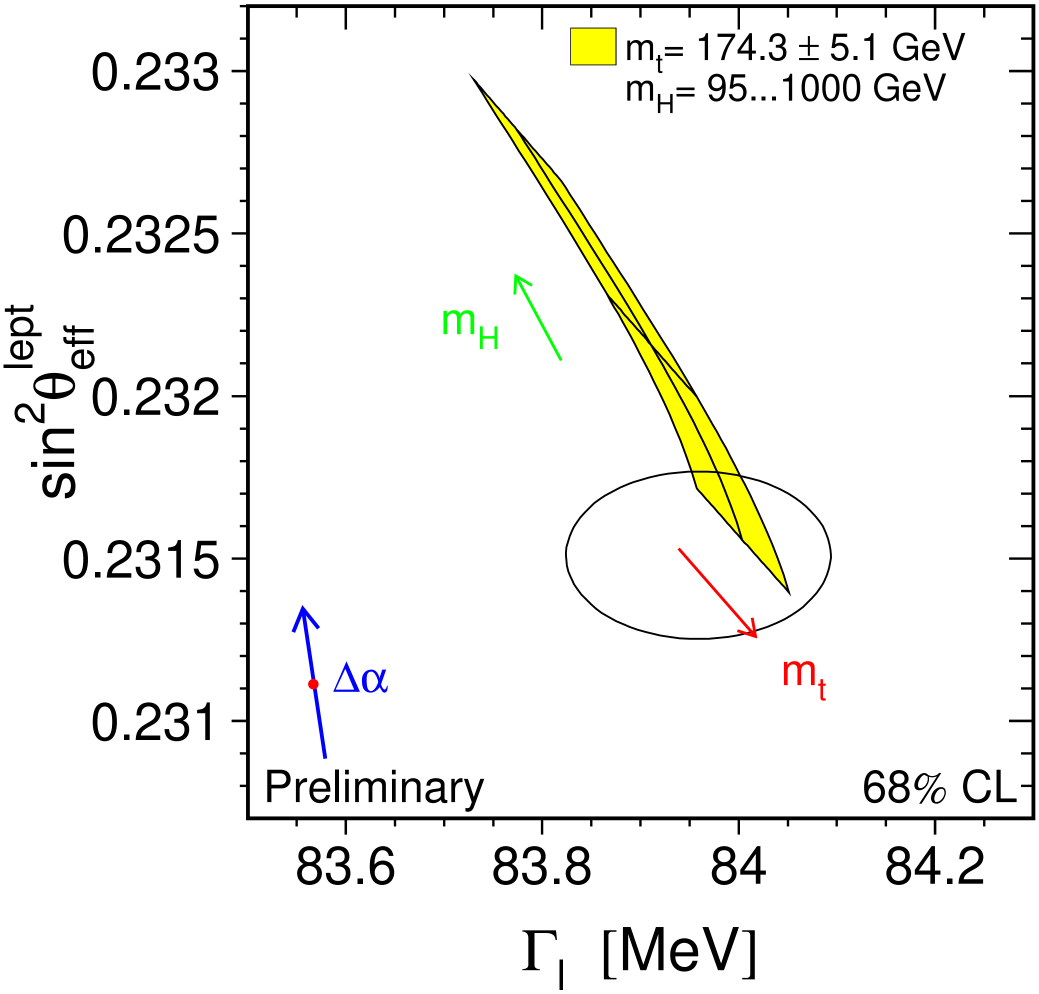

FIG. 5. LEP-I+SLD measurements of $\sin^2\theta_{eff}^{lept}$ and Γ_{ll}, the leptonic width of the Z, and the Standard Model prediction. The point shows the predictions where among the electroweak radiative corrections only the photon vacuum polarization is included. The corresponding arrow shows the variation of this prediction if $\alpha_{EM}(M_Z^2)$ is changed by one standard deviation. This variation gives an additional uncertainty to the Standard Model prediction shown in the figure.

We take as our goal the reduction of error on $\Delta\alpha_{had}^5(M_Z^2)$ (from the integral in Eq. 2) in our kinematic region to a level below that in other kinematic regions as shown in ref. [8]. 1) For $1.4 < \sqrt{s} < 2.0$ GeV, the region below the range of BES, we will reduce the error to about 0.3×10^{-4}. This implies that the error on the integral over R in Eq. 2 will be less than 3%, an improvement of about a factor of 5 over the current uncertainty. 2) For $2.0 < \sqrt{s} < 2.5$ GeV which is covered by the preliminary BES-II results, we will reduce the current error by about a factor of two. This region has the second biggest contribution to the total error. The overall uncertainty on $\Delta\alpha^5_{had}(M_Z^2)$ would then be about 0.00013, giving $\delta M_H \sim 5$ GeV.

2. $g_\mu - 2$

Theoretically the anomalous g value is the simplest quantity calculable to extremely high precision in the standard model. The comparison of precise measurements of $a_\mu = (g_\mu - 2)/2$ with theory thus provides a crucial test of the standard model [15] and may open up a window for new physics. The goal of the current $g_\mu - 2$ experiment at Brookhaven National Laboratory [15] is to reach a precision of 4×10^{-10} and substantial progress has been made [16]. It is now necessary to calculate a_μ to even greater accuracy than before.

In the standard model [3], we have $a_\mu = a_\mu^{QED} + a_\mu^{weak} + a_\mu^{had}$, where a_μ^{QED} and a_μ^{weak} are known to a few parts in 10^{-11}. The contribution of the hadronic vacuum polarization to a_μ^{had} can be calculated by [3,17]

$$a_\mu^{had} = \frac{\alpha^2(0)}{3\pi^2} \int_{4m_\pi^2}^{\infty} ds \frac{K(s)}{s} R(s) \tag{3}$$

$$K(s) = x^2(1 - \frac{x^2}{2}) + (1-x)^2(1 + \frac{1}{x^2})(\ln(1+x) - x + \frac{x^2}{2}) + \frac{(1+x)}{(1-x)} x^2 \ln x, \tag{4}$$

where $x = (1-\beta_\mu)/(1+\beta_\mu)$ and $\beta_\mu = \sqrt{1 - 4m_\mu^2/s}$. The greatest contribution comes from the low energy part of the integral with $\sim 92\%$ coming from $\sqrt{s} < 1.8$ GeV [3]. The current value, $a_\mu^{had} = (695.1 \pm 7.5) \times 10^{-10}$, has an error twice as big as the goal of the BNL experiment. Thus the kinematic region $1.4 < \sqrt{s} < 2.5$ GeV is critical. The contribution to a_μ^{had} from this range is $\sim 4 \times 10^{-9}$. Reduction of the error in this region to $\sim 1 \times 10^{-10}$ requires an accuracy in the R measurement of 2.5%.

3. **Summary**

We propose a measurement of R in the energy range $1.4 < \sqrt{s} < 2.5$ GeV at a precision of 2.5%. This will allow the calculation of $g_\mu - 2$ to an accuracy better than the projected experimental uncertainty of the BNL experiment, leading to a stringent test of the standard model. The measurement will lead to a reduced uncertainty in $\alpha_{EM}(M_Z^2)$ which will reduce the currently large uncertainty in the calculated mass of the Higgs to less than 5 GeV. It is worth noting that at PEP-N we will have the excellent knowledge of the center of mass energy essential for the accurate measurement of R, both from beam diagnostics and from the measurement of thresholds for $N\bar{N}$ and $\Lambda\bar{\Lambda}$.

B. Nucleon form factors

The form factors of the proton and neutron are fundamentally important in that they describe the bound state properties of three valence quarks in the configuration that dominates the known baryonic matter in the universe. The form factors embody the probability that a nucleon will remain intact after absorption of a virtual photon with four-momentum transfer Q^2, as shown in Fig. 6, where we define the form factors to be space-like for $Q^2 < 0$, and time-like for $s = Q^2 > 0$. In Appendix I we give the differential cross section for $e^+e^- \rightarrow N\overline{N}$ in terms of the form factors and provide some further discussion of kinematics.

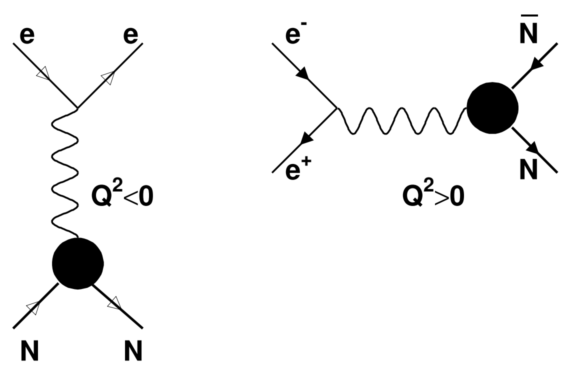

FIG. 6. Feynman diagrams containing the nucleon form factors

Confronting nucleon form factor data with QCD-based models of quark bound states is one of the most important ways of pinning down parameters of the models, which then can be used to predict other observables. At small Q^2 the form factors can be thought of as describing the distribution of charge and magnetization current within the nucleons, while at high Q^2 they probe the valence quark distribution functions at high relative momentum [18,19], with the dominant Feynman diagram being the exchange of two gluons. As QCD models develop, and are able to predict phenomena over the full range of Q^2, from the non-perturbative regime near threshold to the perturbative regime at very large Q^2, nucleon form factor data will be crucial in testing the validity and applicability of these approaches to solving QCD.

A great deal of effort has been put into elucidating the form factors in the space-like region, with ongoing efforts at several laboratories to improve the separate determinations of both electric and magnetic form factors of both the proton and neutron over an increasingly large Q^2 range, and also to determine the form factors of strange baryons.

Much less is known about the time-like form factors. Even so, many questions have been raised by the existing data [20] and there is clearly a strong case [21] [22] to be made for new measurements of the neutron time-like electric and magnetic form factors. In addition, measurements that separate the electric and magnetic (or equivalently the Pauli and Dirac) form factors of the proton are called for by the surprisingly strong variation with Q^2 of the existing data near threshold, in which the form factors were not separately measured. This strong Q^2 dependence may be related to the narrow structures observed in multihadronic cross sections near the $N\overline{N}$ threshold. For this reason it is important to make improved measurements of multihadronic cross sections with good energy resolution in a variety of channels in addition to measuring the nucleon form factors.

At present, predictions of nucleon form factors are applicable to high $|Q^2|$ in both the spacelike and timelike regions. Analyticity relates timelike and spacelike form factors, predicting a continuous transition and spacelike-timelike equality at asymptotic $|Q^2|$. This behavior is also found by PQCD [18,19], which in addition predicts $F_1(Q^2) \propto \alpha_S^2(Q^2)/Q^4$ and $F_2(Q^2) \propto \alpha_S^2(Q^2)/Q^6$. Here $\alpha_S(Q^2)$ is the strong coupling constant, $F_1(Q^2)$ is the non-spin flip form factor and $F_2(Q^2)$ is the spin flip form factor, which decreases with an extra power of $1/Q^2$ due to helicity conservation. Both PQCD [23,24] and analyticity [25] predict that the ratio of neutron to proton form factors is < 1, namely $(G_M^n/G_M^p)^2 \sim (q_d/q_u)^2 \sim 0.25$ in both the timelike and spacelike regions. This prediction is expected to hold in the threshold region based on PQCD and dispersion relations [21,22], and the known vector meson spectrum.

There are several unexpected experimental features in the existing data for timelike form factors that motivate the need for a new high statistics experiment with the ability to separately measure the electric and magnetic form factors (or equivalently F_1 and F_2). These are summarized as follows:

- Ratio between neutron and proton form factors: The measurements of the neutron magnetic timelike form factors are shown in Fig. 7, as obtained primarily by FENICE [20]. Two further measurements by DM2 at DCI are included [26], at $Q^2 = 5.75$ GeV^2 on the basis of two candidate events, and from the Λ timelike form factors according to U-spin invariance (that is $G_M^n \sim 2G_M^\Lambda$) [27]. Remarkably, the neutron magnetic form factor is found to be larger than that of the proton, at variance with the predictions of most models. Calculations in which the form factors are largely determined by valence quarks have great difficulty in predicting such a large neutron magnetic form factor. Large neutron to proton form factor ratios have been predicted by using rather extreme parameters in several effective low-energy VDM [28] and Skyrme [29] models.

  One factor responsible for the large experimental neutron to proton form factor ratio may be the simplifying assumption required to extract G_M from the experimental cross sections (i.e. $G_M^n = G_E^n$ and $G_E^p = G_M^p$) These statements are exact at threshold, (see Appendix I) but may be poor approximations above threshold). A new high statistics measurement is needed to separate electric and magnetic form factors in order to obtain an *ansatz*-free determination of the ratios G_M^n/G_M^p and G_E^n/G_E^p as a function of Q^2.

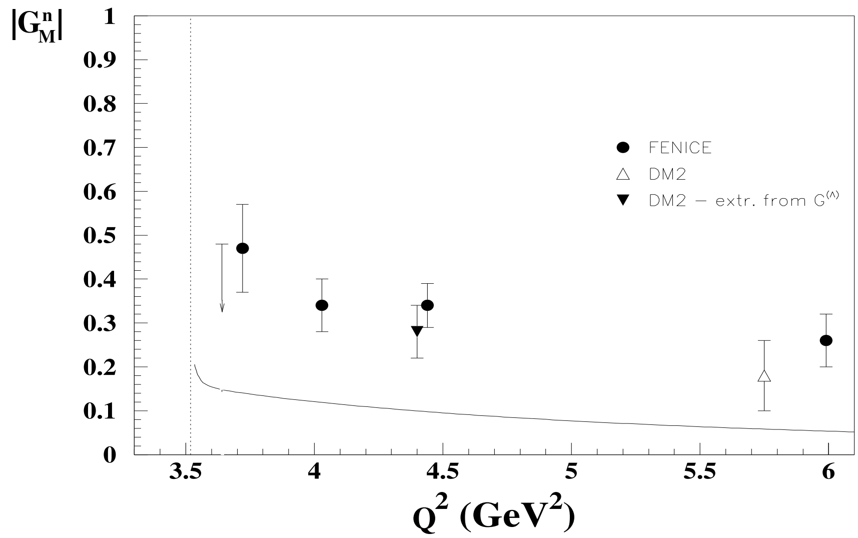

FIG. 7. Neutron magnetic form factor in the timelike region. The data are from [20], [26], [27]. The solid line represents a PQCD based prediction for the asymptotic behavior $|G_M^n| = 0.5||G_M^p|$. The dotted line indicates the $n\overline{n}$ threshold.

- Threshold Q^2 dependence: The proton magnetic form factor has a rapid fall with Q^2 just above threshold. This result was achieved by the PS-170 experiment at LEAR [30]. The data are shown in Fig. 8(a). For the neutron, there may also be a strong fall with Q^2 above threshold. The existing statistics-limited data from FENICE [20] are more compatible with a non-isotropic than an isotropic angular distribution, suggesting that $G_M^n \gg G_E^n$ in the accessible energy range. Since at threshold the relationship $G_M(4M^2) = G_E(4M^2)$ (see Appendix I) is exact, this result may result from a rapid decline of G_E^n with increasing Q^2. On the other hand, if G_M^n and G_E^n are actually comparable such that their ratio has a weak Q^2-dependence (that is $G_E^n \sim G_M^n \sim 0.35$ at 4 GeV^2), the existing data imply a very large ratio of timelike to spacelike electric form factor at $|Q^2| = 4$ GeV^2, as the existing spacelike data are consistent with $G_E^n(-4M^2) \sim 0$.

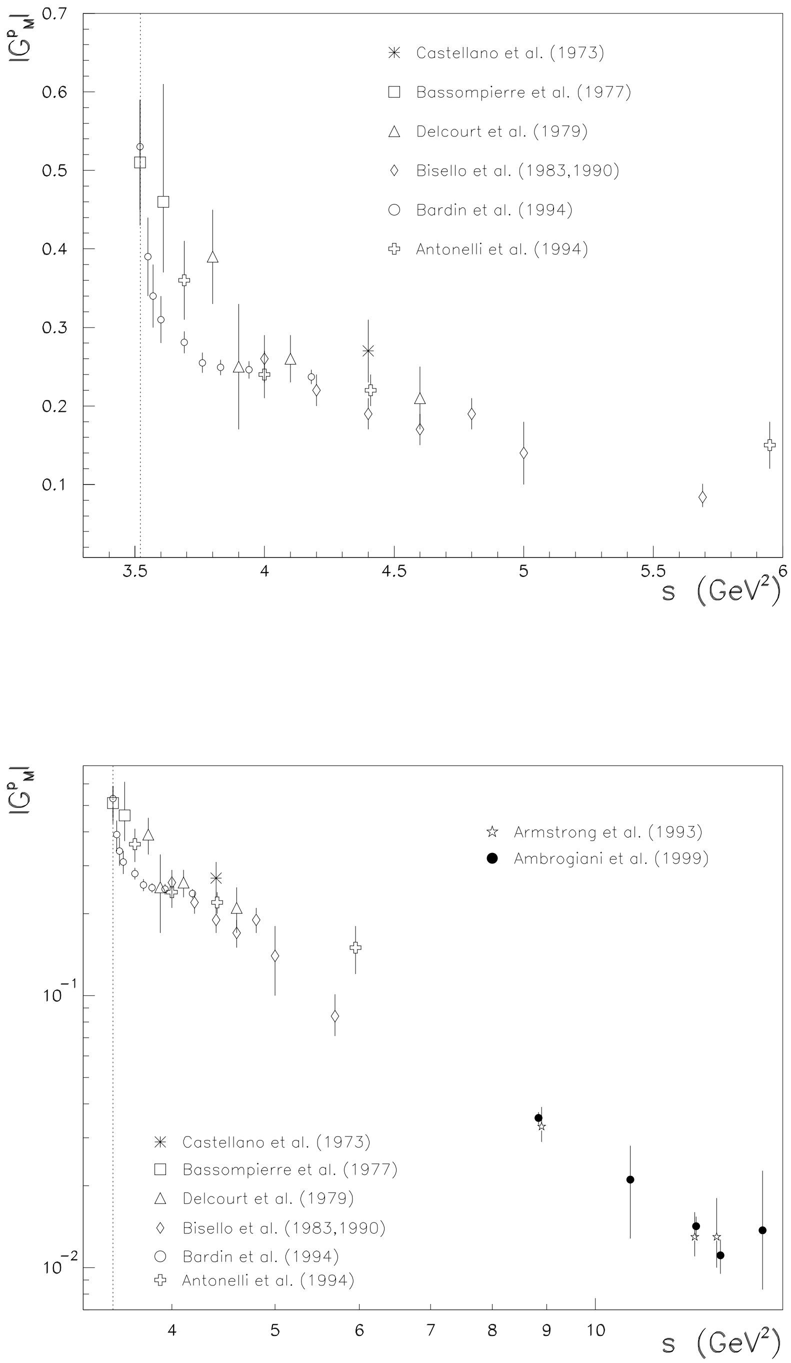

FIG. 8. Proton timelike form factor: (a) low $|Q^2|$, (b) high $|Q^2|$. The dotted line indicates the $p\overline{p}$ threshold. See [31] for experimental references.

- High $|Q^2|$ predictions: In the Q^2 range explored to date, the high Q^2 prediction of equality of spacelike and timelike form factors at fixed $|Q^2|$ remains unsatisfied, with the proton magnetic timelike form factor remaining substantially larger than the spacelike form factor measured at the same $|Q^2|$. The various measurements of the proton magnetic timelike form factor [30,31] are shown in Fig. 8. The expected high Q^2 behavior $1/Q^4$ [32] is reached quite early, however there is a factor of two between timelike and spacelike form factors measured at the same $|Q^2|$. The same factor is observed in the pion form factor; in this case a qualitative explanation has been suggested in an improved PQCD analysis in terms of integrable singularities of the propagators [33]. Disentangling electric and magnetic form factors would permit a better understanding of the high Q^2 behavior.

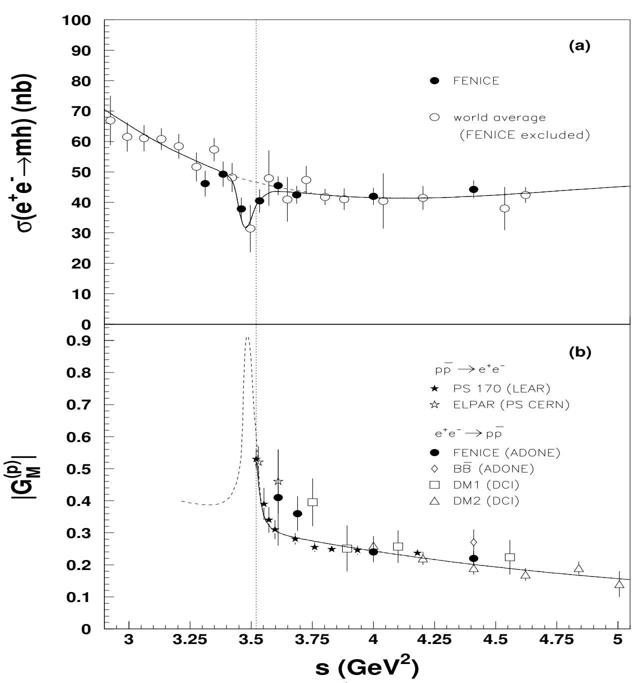

FIG. 9. (a) Total multihadronic cross section (FENICE data and the average over previous experiments) superimposed on the result of a fit to a narrow resonance below the $N\overline{N}$ threshold; (b) comparison of the proton FF data to the expected behavior for such a resonance. The dotted line indicates the $p\overline{p}$ threshold.

- Resonant structures: The steep Q^2-dependence of the proton form factor near threshold suggests a relatively narrow structure below threshold, which would be seen also in multihadronic e^+e^- annihilation near the $N\overline{N}$ threshold [34]. Anomalies are indeed seen in the total cross section $\sigma_{tot}(e^+e^- \to hadrons)$ (see Fig. 9a) and in some multihadronic e^+e^- annihilation channels. Fig. 10 shows the structure observed by DM2 in the $e^+e^- \to 6\pi$ channel, which is the multihadronic channel with the largest cross section at these c.m. energies.

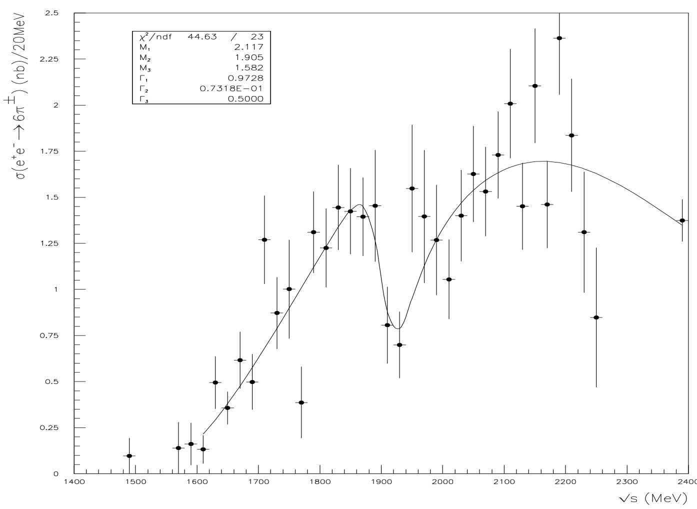

FIG. 10. Cross section for $e^+e^- \to 3\pi^+3\pi^-$ measured by the DM2 experiment.

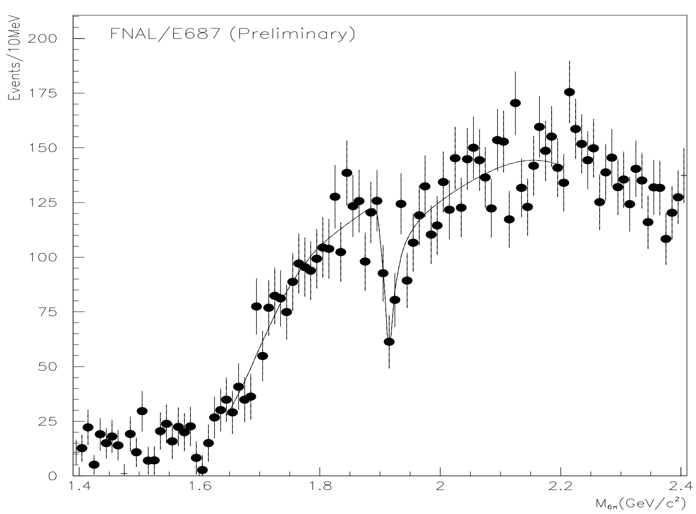

FIG. 11. $3\pi^+3\pi^-$ invariant mass distribution in high energy diffractive photoproduction by FNAL/E687 (preliminary). The mass resolution has been unfolded and a $1/M$ factor is applied to the E687 data to facilitate comparison with e^+e^-.

A remarkably similar structure is seen in high energy diffractive photoproduction, a process closely related to e^+e^- annihilation. The structure shown in Fig. 11 is observed in diffractive photoproduction of $3\pi^+3\pi^-$ by FNAL E687 in a high statistics, high mass resolution data set and also by Fermilab E831 [41]. Other narrow structures are potentially present in channels present in the same data samples.

The dip in the total multihadronic cross section and the steep variation of the proton form factor near threshold (see Fig. 9) may be fitted with a narrow vector meson resonance, with a mass $M \sim 1.87$ GeV and a width $\Gamma \sim 10-20$ MeV. The relatively small cross section and width suggest that the couplings of this state to e^+e^- and to multihadronic channels are small. Its influence may be manifested by mixing with a broad nearby vector meson, as shown in (Fig. 12). In this case the corresponding amplitude has a dip at $\sqrt{s} = M_0$, as demonstrated [35] in a different context :

$$A \propto \frac{1}{s - M_V^2} \cdot (1 + a\frac{1}{s - M_0^2}a\frac{1}{s - M_V^2} + ..) \propto \frac{s - M_0^2}{(s - M_V^2)(s - M_0^2) - a^2}.$$

Here the complex masses M_V and M_0 contain the masses and widths of the broad vector meson V and narrow resonance V_0; a is the V_0V coupling constant.

Such a narrow resonance would be consistent with a $N\overline{N}$ bound state (Fig. 12). Such states have been predicted [36–40] and some sightings have been reported. However such states have not been confirmed experimentally. The e^+e^- annihilation data described here are compatible theoretically with existing data for $N\overline{N}$ annihilations.

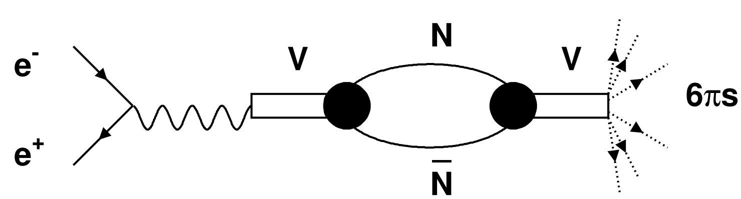

FIG. 12. Diagram describing the e^+e^- annihilation via an intermediate $N\overline{N}$ bound state.

Additional high-statistics, high-mass-resolution e^+e^- annihilation data in the mass range $1.4 < \sqrt{s} < 3$ GeV are clearly needed to confirm these effects, determine the masses and widths of these putative new vector mesons and determine their relationship with the nucleon form factors.

- Overall analytic solution for nucleon form factors: The nucleon form factor in the unphysical region below the $N\overline{N}$ threshold, where the structures discussed above would appear, can in principle be calculated from the spacelike form factor using dispersion relations and many such attempts have been made; one such solution is shown in Fig. 13.

  Unfortunately, a stable solution cannot be obtained without a huge and unrealistic improvement in statistical accuracy with respect to the existing spacelike data. However modestly accurate data in the timelike region will in principle allow a stable solution. A recent evaluation of the magnetic form factors in the unphysical region [42] shows unexpected features, potentially related to structures of the type discussed above, which can realistically be resolved only by new data in the timelike regime.

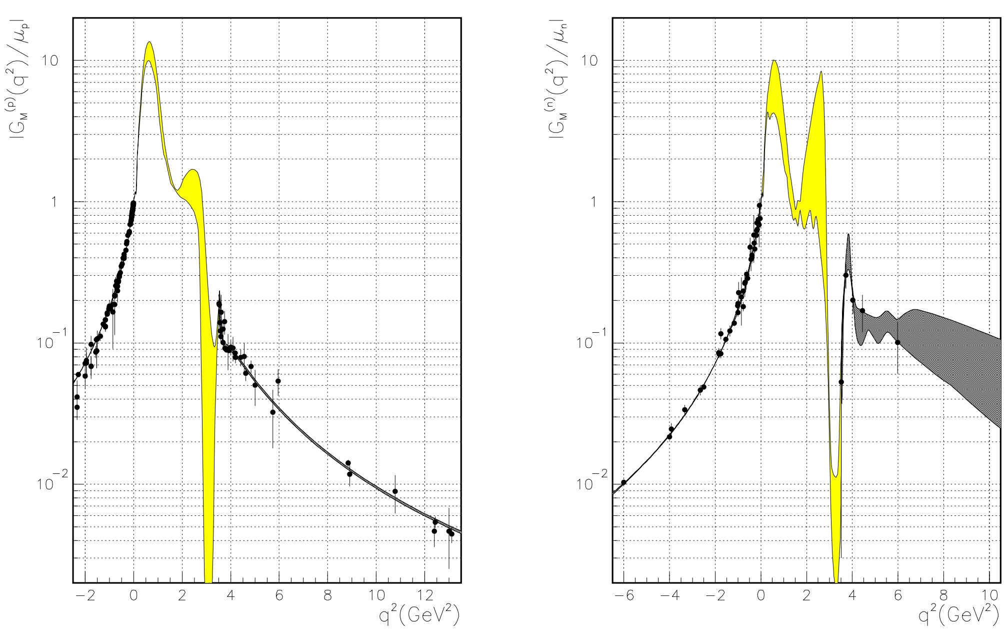

FIG. 13. Proton (a) and neutron (b) magnetic form factor in the unphysical region from dispersion relations.

These considerations strongly support the importance of a new measurement of the neutron and proton timelike form factors with much higher statistics than previous work and with the capability of seperately determining the electric and magnetic form factors, especially very close to threshold. Such a new measurement would significantly improve our knowledge of the form factors in the unphysical region and would check the consistency of spacelike measurements.

It is worth noting that for the proton form factor, the alternative technique of antiproton annihilation suffers from complications related to stopping $\overline{p}$'s in a target [44]. A measurement at a e^+e^- collider avoids these difficulties, albeit at the expense of a smaller cross section.

Near and below the threshold a measurement of the various multihadronic e^+e^- channels is also of great importance to understand if there are indeed $N\overline{N}$ bound states. We propose a statistical accuracy comparable to that achieved in diffractive photoproduction. e^+e^- annihilation provides a much better mass resolution than photoproduction which is particularly important to a search for narrow structures.

C. Other baryon form factors

Nucleon excitation via electron scattering demonstrates three prominent resonant regions, at 1.232, 1.535, and 1.65 GeV. The first is due to the $\Delta(1232)$ resonance, and the other regions each represent the overlap of several resonances. Electron scattering (spacelike) data to $Q^2 \sim 20$ GeV^2 has been analyzed in terms of transition form factors, analogous to the nucleon form factors discussed above [43]. The magnitudes of the transition form factors are comparable to those of the nucleon form factors. Perturbative QCD predicts a $1/Q^4$ dependence for the transition form factors, which is satisfied for the higher mass resonances.

However the transition form factor for the Δ resonance falls much faster, approximately as $1/Q^6$, which may be due to suppression of the leading-order PQCD amplitude, leaving higher-order amplitudes dominant.

Time-like data will be important in testing QCD and in resolving the questions raised by the spacelike Δ data. There appears to be no existing data. The transition form factors are determined by observing annihilations to nucleon plus baryon resonance. We will have access to the Δ in its $N\pi$ and $N\pi\pi$ decay modes and the $S_{11}(1535)$ in its $N\pi$ and $N\eta$ decay modes.

Since the cross sections are expected to be similar, we anticipate experimental errors for the resonance transition form factors that are comparable to those for the nucleon form factors. These uncertainties will easily be small enough to identify the power of the Q^2 dependence. We are hopeful that the angular distributions and polarization data will allow determination of individual form factors, i.e. charge, dipole, quadrupole, for a more detailed study of hadron structures and of QCD predictions.

The physics of hyperon form factors is analogous to that of nucleon form factors. Form factors reveal the distribution of charge and magnetization within the hyperons and probe the quark wave functions of these states. Flavor symmetry relates the hyperon form factors to those of the nucleons and accurate prediction of flavor-symmetry breaking is an important test of QCD. At PEP-N we will measure the form factors of the Λ, Σ^0 and charged Σ. We will also determine the $\Lambda - \Sigma^0$ transition form factor, which is different from the N-Δ transition form factor discussed above in that the baryons are members of the same SU3 multiplet.

D. Meson form factors

Hadron form factors fall into the category of exclusive reactions at non-asymptotic momentum transfers. Computation of hadron form factors is a critical test of QCD and there is an active program in form factor computation using perturbative QCD, which is expected to be accurate at asymptotic Q^2, but is however not yet fully successful at accessible Q^2. There is active interest in the question of whether these processes can be successfully described by perturbative QCD at experimental Q^2 or whether these fundamental properties of hadrons are intrinsically non-perturbative in this regime [24]. Much of the theoretical attention has been directed at the proton form factor because of its experimental accessibility in both spacelike and timelike regimes. However the meson form factors are intrinsically simpler and may provide more guidance to theory than nucleon form factors.

For the pion form factor and for the charged and neutral kaon form factors, there is relatively sparce data only at the very small spacelike momentum transfers $Q^2 < 0.25$ GeV^2 and for timelike momentum transfers smaller than 2.0 GeV^2. Despite this, a significant amount of sophisticated theoretical work has been done which has not been afforded comparison with experiment. Although much better measurements of the pseudoscalar spacelike form factors are not likely to be available soon, the fact that analyticity implies that high-statistics measurement of the timelike form factor determines the spacelike form factor makes it possible to comprehensively compare experiment with theory.

We are aware of no work, either experimental or theoretical, on form factors of vector mesons. A significant difficulty in vector meson form factors is the large cross section for competing processes leading to the same final state. Successful prediction of pseudoscalar and vector meson form factors are necessary elements of a comprehensive description of hadron structure. The PEP-N experiment will have the capability of observing formation of pairs of charged pions, charged rho mesons and charged and neutral K and K* mesons. It will have the capability of making precise measurement of the electromagnetic form factors for the π and K mesons hadrons in the (timelike) regime 1.4 GeV$< \sqrt{s} <$ 2.5 GeV. If backgrounds permit it will be able to make the first measurements of vector meson form factors.

A closely related area is the 3-point coupling of a vector meson, pseudoscalar meson and photon, manifested in e^+e^- annihilation to $\rho\pi$, $\omega\pi^0$, $\phi\pi^0$, analogous reactions with η's, and annihilation to K^*K, each dependent on an s-dependent transition form factor. These fundamental processes are potentially amenable to perturbative QCD in this regime.

E. 1^{--} spectroscopy

A hadron pair made in electron positron annihilation is necessarily in a neutral 1^{--} state and these reactions therefore constitute the simplest arena in which to study 1^{--} states, as it is straightforward to determine the reaction amplitude. An analysis of this type was carried out by Donnachie and Mirzaie [45], who found evidence for the $\rho(1450)$ and $\rho(1700)$. Exclusive multihadron channels may also be analyzed for the formation of vector mesons as described below. The PEP-N experiment will generate high-statistics data in channels containing multiple π and K mesons that can be analyzed for the formation of heavy ρ, ω, and ϕ mesons. While eight such mesons have been given PDG status [46], $\omega(1420)$, $\omega(1600)$, $\omega_3(1670)$, $\phi(1680)$, $\rho(1690)$, $\phi_3(1850)$ along with the 2 heavy ρ mesons noted previously, the branching modes of these resonances are very poorly known and improved determinations are possible at PEP-N. In addition to determination of masses and other parameters of vector states, the measurement of cross sections for e^+e^--annihilation into isovector final states allows testing of the Conserved Vector Current hypothesis (CVC), which relates these processes to the $\tau \to \nu$+hadrons decays.

The existing experimental data are at energies below $2E < 2$ GeV obtained at the DCI and VEPP-2M colliders. The DM1 and DM2 detectors at DCI finished data taking more than 10 years ago with an integrated luminosity of about 4 pb^{-1}, while experiments at VEPP-2M in the energy range $2E < 1.4$ GeV were finished in 2000. The integrated luminosity collected at VEPP-2M in the energy range $2E = 1.0 - 1.4$ GeV by two detectors CMD-2 [47] and SND [48] is ~ 20 pb^{-1}. The VEPP-2M ring will shortly be removed making room for the new VEPP-2000 collider with a maximum energy $2E = 2$ GeV.

We describe some of the results from DCI and VEPP-2M.

1. $e^+e^- \to \pi^+\pi^-\pi^0$. This process is interesting from the point of view of detemination of parameters of the excited isoscalar resonance ω' decaying into 3π. The PDG [46] parameters of this state are not well established. Old measurements at VEPP-2M [49] and DM2 [50] gave an average cross section $\sigma_{3\pi} \simeq 3$ nb. In 1999 more accurate

data from the SND experiment shown in Fig. [51] were published. A broad peak at $2E \simeq 1200$ MeV was observed in the $\pi^+\pi^-\pi^0$ production cross section. Combined fitting of the SND data together with the old DM2 data [50] gives ω' parameters which are strongly model-dependent. The mass varies from 1200 to 1500 MeV and the width from 200 to about 900 MeV. To reduce model dependence precision data at energies above 1.4 GeV are needed. Such data can be obtained at PEP-N or VEPP-2000.

2. $e^+e^- \to \pi^+\pi^-\pi^0\pi^0$, $e^+e^- \to \pi^+\pi^-\pi^+\pi^-$.

   These reactions give the largest contribution into the isovector part of the hadronic production cross section in the region of $2E \simeq 1.5$ GeV. In the past these processes were studied at VEPP-2M [49,52] DCI [53], and ADONE [54]. The statistical accuracy achieved in these experiments is $\sim 5\%$, but experimental data (Figs. 15, 16) show significant systematic errors which are sometimes above $\geq 20\%$. On the basis of these data together with measurements of $e^+e^- \to \pi^+\pi^-$ and $e^+e^- \to \omega\pi^0$, Donnachie et. al [55] concluded that yet another ρ excitations at about 1600 MeV exists: The parameters of all of the vector excitations are still poorly determined and new measurements with smaller systematic errors are needed to clarify this problem.

   Recently CMD-2 made an analysis of intermediate states in the reaction $e^+e^- \to 4\pi$ below 1.4 GeV [56]. It was shown that two intermediate states: $\omega\pi^0$ and $a_1\pi$ completely saturate the total cross section of this process. It would be interesting to extend such analyses to higher energies.

3. $e^+e^- \to \omega\pi^+\pi^-$. This reaction, studied by DM2 [50], determines the PDG parameters of the $\omega(1600)$ meson. Recent data from CMD-2 [57] for energies up to 1.4 GeV on the low energy slope of $\omega(1600)$ agree with the DM2 results (fig. 17). More accurate measurements at higher energies are required to pin down the parameters.

4. $e^+e^- \to \eta\pi^+\pi^-$ This reaction is important for determination of parameters of the isovector ρ'-family resonances. The DM2 measurements [50] showed that there is a

wide $\rho(1600)$ peak (fig. 18). One could see that new more accurate measurements are desirable to improve the accuracy of fits. CMD-2 results [57] have much higher accuracy but cover only low energy region (fig. 18).

5. $e^+e^- \to K\bar{K}, K\bar{K}\pi$ Exclusive hadronic reactions with kaons in the final state have considerable cross sections $\sigma \geq 1$ nb and are an important source of information about the ϕ' family of resonances. One such resonance, the $\phi(1680)$ meson, was studied in both photoproduction and in colliding beams experiments DM1 [58] and DM2 [59]. The mass ansd width of this state were measured. However except for the dominant decay mode $K\bar{K}^\star + c.c.$ the other decay modes are poorly measured. More detailed study of the $\phi(1680)$ state is feasible at PEP-N.

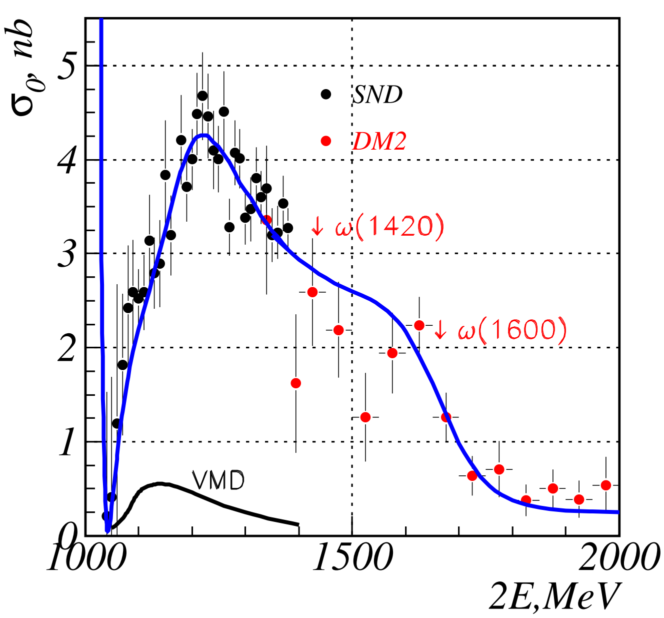

FIG. 14. $e^+e^- \to \pi^+\pi^-\pi^0$ cross section

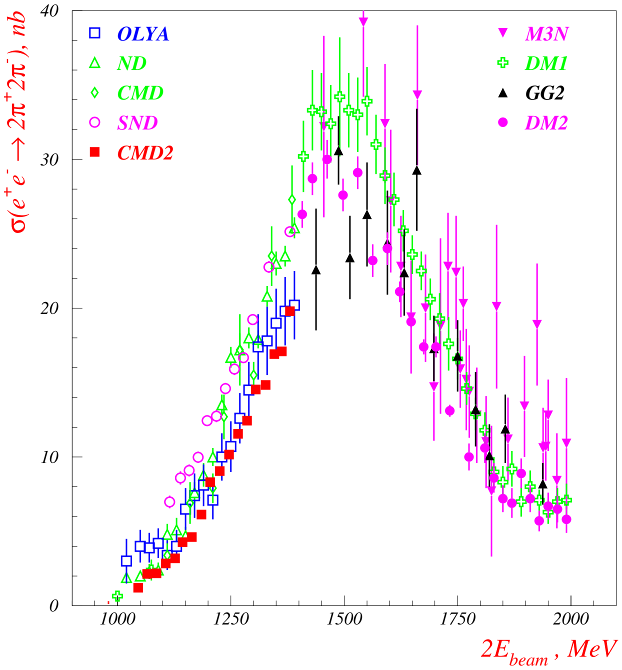

FIG. 15. $e^+e^- \to \pi^+\pi^-\pi^+\pi^-$ cross section

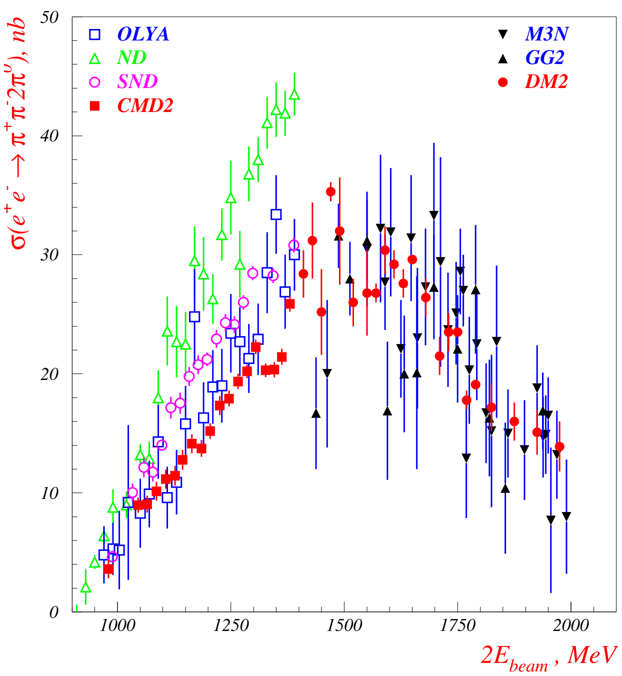

FIG. 16. $e^+e^- \to \pi^+\pi^-\pi^0\pi^0$ cross section

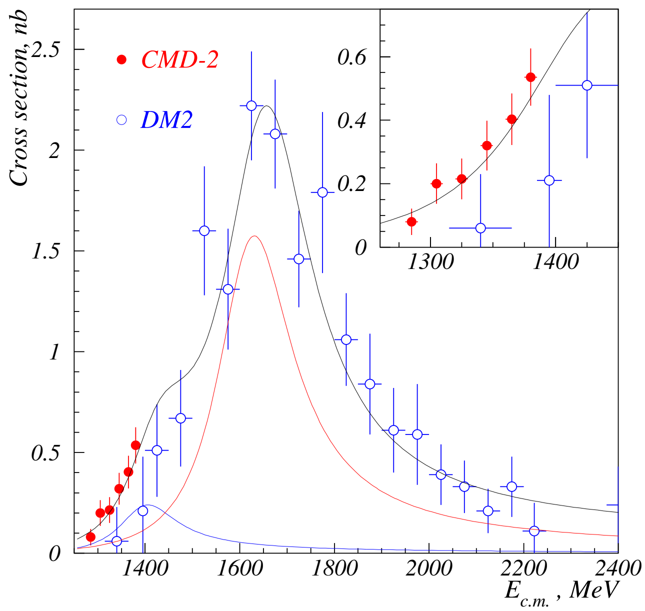

FIG. 17. $e^+e^- \to \omega\pi^+\pi^-$ cross section

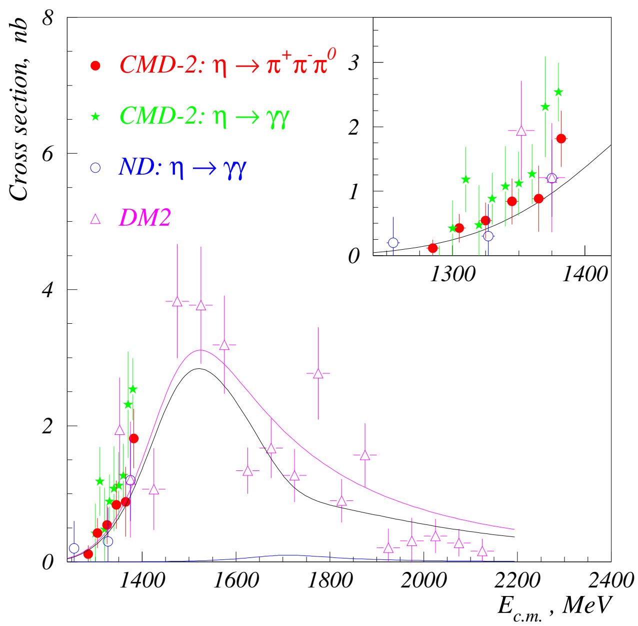

FIG. 18. $e^+e^- \to \eta\pi^+\pi^-$ cross section

F. Production of meson resonances and multihadron channels

Meson resonances including glueballs and other exotics will be sought in production reactions. The nearly 4π center-of-mass coverage will make it possible to sample the entire kinematical region (e.g. Dalitz plot for 3 bodies) and to perform a multibody amplitude analysis. Electron-positron annihilation has the advantage that the overall state is 1^{--} which tightly constrains the analysis, especially for the relatively low center of mass energies and large multiplicities of the reactions of interest. In this sense the analysis is similar to those carried out in antiproton-proton annihilations at rest at LEAR, where mainly S waves are expected, but is even further constrained. However the physics of these electron-positron and proton-antiproton annihilation processes are very different. In antiproton annihilations gluons are abundant; in positron annihilations there are few gluons. It will be interesting to compare resonance production in the two reactions, which may then help to identify putative exotic states such as the $f_0(1500)$ tentatively identified by the Crystal Barrel collaboration as a glueball [60] and the $\eta(1295)$, $\eta(1400)$, $\eta'(1460)$, $f_2(1565)$, $f_2(1640)$, $f_2(1720)$, $f_2(2200)$, states for which accurate placement into SU3 nonets has not yet been achieved.

The dynamics of e^+e^- annihilations in the PEP-N energy regime is not fully understood. One example is the step in R of ~ 0.5 at $\sqrt{s} \sim 2$ GeV which corresponds to no known threshold. Study of multihadronic channels may reveal the source of this and other phenomena.

G. $\gamma\gamma^*$ interactions

$\gamma\gamma^*$ interactions are obtained by studying hadroproduction in e^+e^- scattering. Meson production and production of particle-antiparticle pairs in both single-tag and double-tag modes constitute tools for studying the quark-gluon structure of the hadrons and testing the capabilities of QCD in its various formulations. The initial theoretical work in this area was the calculation of single pseudoscalar meson production by Brodsky and Lepage [19] in the Light Cone Approach. Good agreement with theory was observed for $\gamma\gamma^*$ production of π^0 η, and η' (i.e. the pseudoscalar meson-photon transition form factor) in experiments at CLEO [62].

Work in perturbative QCD [61] has shown that the process $\gamma\gamma^* \rightarrow h\bar{h}$ in the kinematical domain $W^2 << Q^2$, the continuation of deeply virtual Compton scattering from hadrons, where W^2 is the center of mass energy and Q^2 is the γ^* virtuality, factorizes into a calculable hard scattering amplitude to partons (quark-antiquark or gluon-gluon)and a non-perturbative amplitude for hadronization. The production of a pair of pseudoscalar mesons has been calculated.

In the PEP-N kinematic regime, the processes satisfying the condition $W^2 << Q^2$are: $\gamma\gamma^* \rightarrow \pi^0$ and $\gamma\gamma^* \rightarrow \pi^+\pi^-$. The former has been measured [62]. Study of the latter process at PEP-N will supply a description of the $q\bar{q} \rightarrow \pi\pi$ process at energies and momentum transfers that are germane to hadroproduction at hadron and electron-positron colliders as well as at neutrino experiments. A further interesting aspect is to test the scaling in Q^2 (the analog of Bjorken scaling for this channel). The helicity structure of the process is predicted by PQCD and can be obtained from the two-pion angular distribution.

Recently, it has been pointed out that one can study the $\gamma\gamma^* \rightarrow \pi\pi$ process (one offshell photon) at the amplitude level through the interference term between $\gamma\gamma^*$ and bremsstrahlung(where a single photon forms a $\pi^+\pi^-$ pair, mainly through intermediate ρ production) subprocesses [63] [64]. One can then completely distinguish the amplitudes A_{++}, A_{+-}, and A_{0+} for different photon helicities. In the kinematical region where the bremsstrahlung is large, the interference term gives the relative phase of these amplitudes with respect to the phase of the pion form factor, known to be the $\pi\pi$ phase shift δ_1.

The $\gamma\gamma^*$ reaction produces $\pi^+\pi^-$ in the C-even channel, and bremsstrahlung leads to $\pi^+\pi^-$ in the C-odd channel. The interference determines the charge asymmetry of the process and disappears when averaged over the pion charge. The interference term can be separated from the pure $\gamma\gamma^*$ and bremsstrahlung contributions in two different ways :

1) It be obtained by reversing the charge of the lepton in the $e\gamma$ collisions; this can be done

with e^+e^- colliders by measuring $\sigma(e^-\gamma \to e^-\pi^+\pi^-) - \sigma(e^+\gamma \to e^+\pi^+\pi^-)$.
2) Alternatively the measurement of the difference between the number of π^+ and π^- mesons makes it possible to measure this interference term.

The time-like pion form factor in the bremsstrahlung term gives the relative weight of the different contributions. It leads to an enhancement of the interference term in a broad energy interval near the ρ mass. For this reason, this process should be investigated in the regime where the invariant mass W of the $\pi^+\pi^-$ system is close to that of the ρ.

Good statistics in a single tag photon mode are available at relatively small Q^2, where the bremsstruhlung process is large and therefore the interference substantial and measurable. The cross section of the process is $\sim$ 8000 fb. The left-right charge asymmetry of the pion pair projects out the interference term [63], yielding a $\sim$ 300 fb cross section (where we have taken $Q^2 > 1$ GeV^2, 300 MeV $<$ W $<$ 1 GeV, the scattering angle of the tagged lepton $<$ 100 mrad, and p_t <500 MeV for the untagged lepton).

The $\pi^0\pi^0$ final state has only a $\gamma\gamma^*$ contribution and therefore no interference. The cross section is $\sim$ 20 fb in the same kinematic region.

Pion pair, kaon pair, proton antiproton and neutron antineutron production for $W^2 \sim Q^2$ are potentially accessible at PEP-N. Although the dynamics in this domain are different from those discussed above, these processes are amenable to the predictions of PQCD and have been analyzed in detail by Brodsky and Lepage [19]. One particularly important topic is pion pair production where the angular dependence of the ratio of $\pi^+\pi^-$ and $\pi^0\pi^0$ differential cross sections gives the dependence of the distribution amplitudes on x, the fraction of the pion momentum carried by the partons.

IV. EXPERIMENTAL CONSIDERATIONS AND DETECTOR CONFIGURATION

The goal of the proposed PEP-N experiment is operation at an instantaneous luminosity $\sim 0.5\times10^{31}\mathrm{cm}^{-2}\mathrm{s}^{-1}$ for a period of approximately 5 years in order to study exclusive channels for form factor, vector meson, etc. measurements as well as inclusive reactions for measuring R. Whether we can do this with a single comprehensive detector or whether two or more separate detectors are required is not yet determined. It is worth noting that the efficient neutron and antineutron detection required only for the neutron form factor measurement has different requirements than the charged particle and photon detection required for the R measurement; the acceptance requirements are different, and the rate for annihilation to all hadrons is roughly 2 orders of magnitude greater than that to $n\bar{n}$. Finally there is clearly no need for a $n\bar{n}$ capability below threshold, where a great deal of the running will be carried out.

We present below some of the basic information required for detector design and *proof of principle* data to show that it is plausible to design an effective experiment at the proposed asymmetical collider. We assume a zero degree collision as described in the accelerator design section, where a very-large-aperture dipole magnet is installed at the intersection, supplying the necessary field integral ($\int Bdl$ = 0.3 T ·m) for bringing together and separating the beams.

A. Rates and running time

The rates for the processes we wish to study vary over a significant range.

The point-like cross-section (e.g. muon pairs) at $\sqrt{s}$ = 2 GeV is 21.7 nb and that for hadrons, taking R$\sim$ 2 is then $\sim$ 43 nb. The cross sections for the processes $e^+e^- \to p\overline{p}$ and $e^+e^- \to n\overline{n}$ are about 1 nb in the energy region of interest, decreasing with center of mass energy $E_{c.m.}$ [20,31]. The cross-sections for $\pi^+\pi^-$ and K^+K^- are about 0.5 nb, that for

$K_L K_S$ about half that and other meson pair cross-sections are expected to be comparable to that for $\pi^+\pi^-$.

Assuming an average luminosity of $5 \times 10^{30} cm^{-2}s^{-1}$ and a detection efficiency of 50 %, the expected event rate for $N\overline{N}$ final states is 200 events per day. A 10 day data taking period at each center of mass $E_{c.m.}$provides about 2000 events per point giving cross-section measurements with statistical uncertainties below 3%. We can expect comparable precisions for other exclusive processes. Under comparable conditions a statistical uncertainties below 1% may be obtained for the multi-hadronic cross-section measurements. Since we wish to explore these processes for narrow structures, we anticipate taking data at intervals no greater than 50 MeV, leading to a total data-taking time of several hundred days. If different experimental configurations are required, one may expect the overall time frame of data taking at PEP-N to be a minimum of several years.

The detector and data acquisition capability should match the highest rate possible in dedicated mode. Taking a maximum total cross-section of 100 nb and maximum possible instantaneous luminosity of $10^{32} cm^{-2}s^{-1}$, the maximum (no background) rate is 10 Hz. Even considering backgrounds, rates should be well below the limit of capability for the detectors we discuss and a modest data acquisition system should suffice.

B. Multihadronic final states

To illustrate the features of multihadronic reactions we have studied by means of a Monte Carlo simulation of $e^+e^- \to 4\pi$ and $e^+e^- \to 6\pi$, in which events are generated according to phase space expectations.

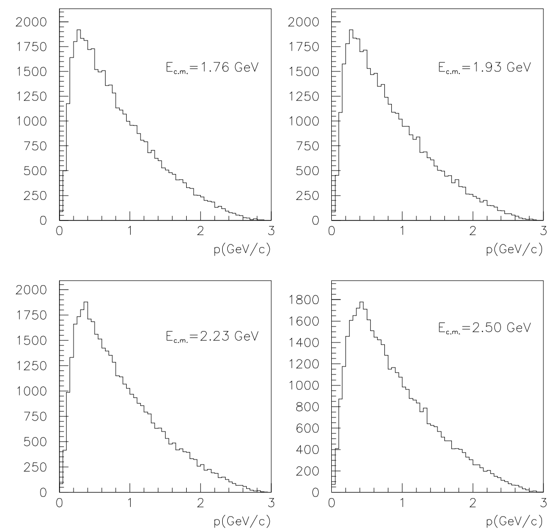

FIG. 19. Momentum distributions for the process $e^+e^- \to 4\pi$ at 4 different c.m. energies.

Fig. 19 shows the momentum distributions in the laboratory frame for the 4π final state and for different values of the c.m. energy. It can be seen that most particles have momenta below 1 GeV, with tails extending up to 3 GeV.

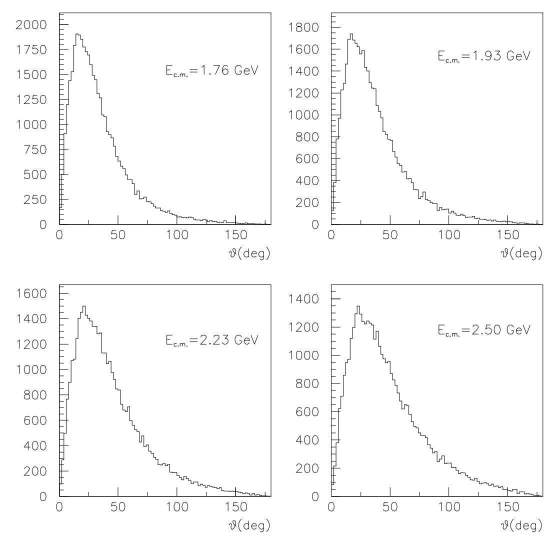

FIG. 20. Polar angle distributions for the process $e^+e^- \to 4\pi$ at 4 different c.m. energies.

Fig. 20 shows the distributions in the laboratory frame polar angle θ (defined with respect to the LER beam direction) for the 4π final state at different c.m. energies. From these distributions we calculate geometric acceptances by requiring at least 3 out of 4 particles to be within a certain θ cut. The results are reported in table I. The table also shows the acceptances for the 6π final state, calculated by requiring at least 5 out of 6 particles to be within a given cut. It can be seen that in order to have a sizeable acceptance the θ coverage of the detector should be of at least 40^o.

$e^+e^- \to 6\ \pi$					
e^- energy (MeV)	E_{cm} (MeV)	θ cut (degrees)			
		30	40	45	50
250	1765	0.10	0.55	0.74	0.87
300	1935	0.03	0.31	0.53	0.69
400	2235	0.006	0.09	0.22	0.38
500	2500	0.002	0.03	0.08	0.19
$e^+e^- \to 4\ \pi$					
e^- energy (MeV)	E_{cm} (MeV)	θ cut (degrees)			
		30	40	45	50
250	1765	0.29	0.69	0.81	0.88
300	1935	0.18	0.56	0.70	0.80
400	2235	0.09	0.33	0.50	0.64
500	2500	0.05	0.19	0.33	0.49

TABLE I. Geometric acceptance for multipion events. In all cases a lower θ cut of 0.5^o is applied to account for the effect of the beam pipe.

C. Nucleon antinucleon final states

The neutrons and antineutrons produced in e^+e^- close to the $n\overline{n}$ threshold are characterized by a very low kinetic energy in the center of mass system ranging between a few MeV and several hundred MeV. Such neutrons are hard to detect with reasonably high efficiency using the same technique for all energies. In this respect the use of an asymmetric configuration where the two particles are boosted forward, each of them taking on average half of the energy of the most energetic beam, is a significant advantage.

In the following we describe the main features of $n\overline{n}$ and $p\overline{p}$ final states in the proposed asymmetric configuration.

1. *Kinematics*

Assuming that we operate with the positron beam (LER) at a fixed energy $E_1 = 3.1$ GeV, and with the electron beam ranging between E_2=250 and 500 MeV, the processes $e^+e^- \to N\overline{N}$ can be studied from threshold, that is $Q^2 = (2 \times M_N)^2 \sim (1.88\ GeV)^2$ corresponding to $E_2 = 285\ MeV$ up to about $Q^2 \sim (2.5\ GeV)^2$ when $E_2 = 500\ MeV$. The dependence of $E_{c.m.}$ on E_2 in this configuration is shown in Fig. 21. Data can be taken below threshold for E_2 between 250 and 285 MeV for background studies.

Due to the boost from the center of mass to the laboratory reference system, the nucleons are emitted in the forward hemispere with momenta ranging from hundreds of MeV to a few GeV. The distributions in polar angle θ_{lab} with respect to the LER beam direction and in momentum p both in the laboratory system are shown for four different values of $E_{c.m.}$ in Figs. 22 and 23 respectively. The distributions are obtained assuming head-on collisions and an isotropic $\theta_{c.m.}$ distribution in the center of mass system.

The θ_{lab} distributions are characterized by sharp peaks at maximum angles θ_{max} whose values increase with $E_{c.m.}$ as shown in fig. 24. We notice that in order to have full acceptance in the energy range allowed by the machine configuration, an angular coverage from about

1^o up to at least 45^o is required. The acceptance for the $N\overline{N}$ final states for various θ cuts are given in Table II.

$e^+e^- \to n\overline{n}$					
e^- energy (MeV)	E_{cm} (MeV)	θ cut (degrees)			
		30	40	45	50
300	1935	0.96	0.96	0.96	0.96
400	2235	0.62	0.98	0.98	0.98
500	2500	0.04	0.26	0.39	0.55

TABLE II. Geometric acceptance for $n\overline{n}$ events. A lower θ cut of 0.5^o is applied to account for the effect of the beam pipe.

Concerning the momentum distributions we observe that the central value corresponds to about $(E_1 + E_2)/2$ at any $E_{c.m.}$. On the other hand the higher the $E_{c.m.}$ the larger the momentum spread. In particular, very close to threshold the particles are emitted at rest in the center of mass system, so each of them gets exactly half the total energy $(E_1 + E_2)$ when they are boosted to the laboratory system.

We stress again that due to the boost, particles with momenta in the GeV range are obtained for all the values of $E_{c.m.}$ even very close to threshold. This is a significant advantage of the asymmetric beam configuration over the symmetric one allowing to use the same detection tecnique for all the values of $E_{c.m.}$.

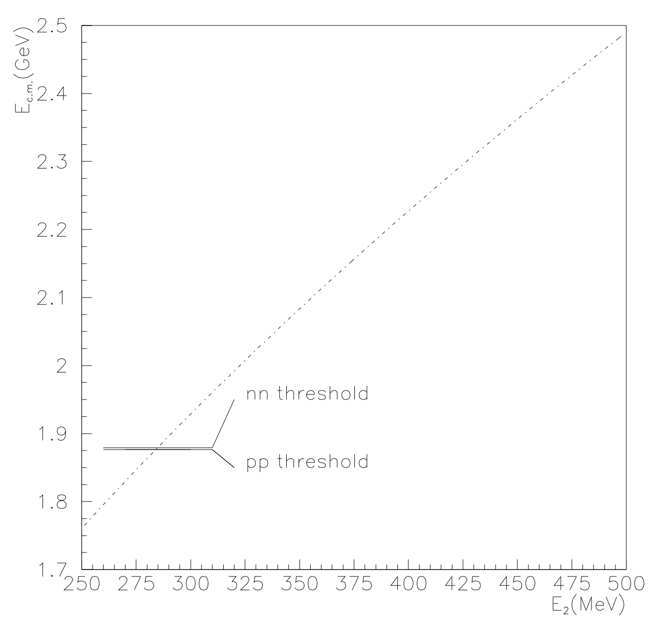

FIG. 21. Center of mass energy $E_{c.m.}$ as a function of the energy E_2 of the electron beam assuming a fixed energy $E_1 = 3.1\ GeV$ of the positron beam. The thresholds for $n\overline{n}$ and $p\overline{p}$ production are shown.

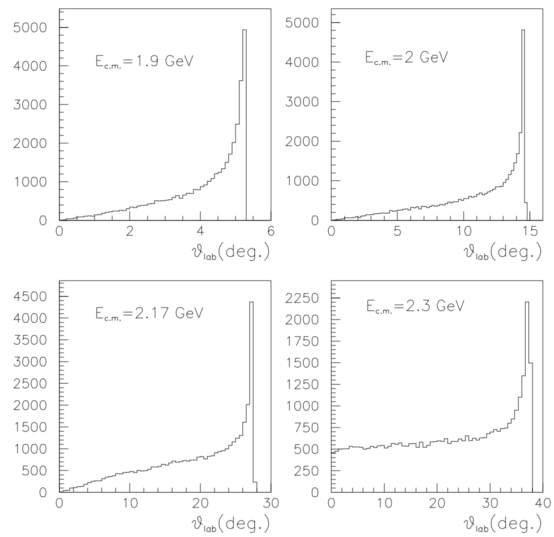

FIG. 22. Examples of polar angle distributions in the laboratory system of nucleons and anti-nucleons at four different center of mass energies.

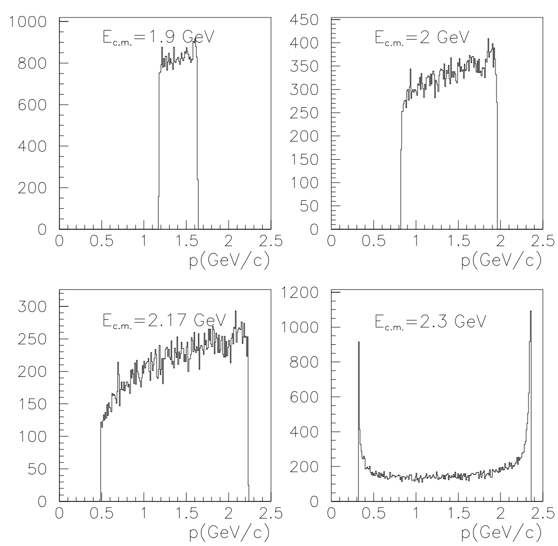

FIG. 23. Examples of momentum distributions in the laboratory system of nucleons and anti-nucleons at four different center of mass energies.

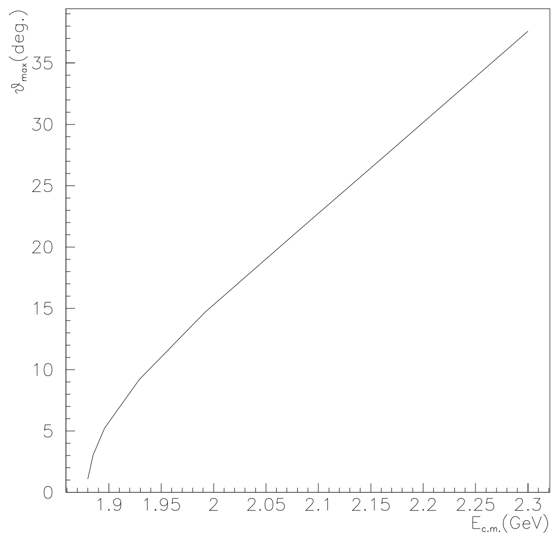

FIG. 24. Maximum angle with respect to the beam direction as a function of the center of mass energy.

2. *Identification and measurement of $N\overline{N}$ final states.*

a. Signatures The main features of $n\overline{n}$ and of $p\overline{p}$ final states are summarized below:

1. There is an angular correlation between the two particles. In the laboratory system the two particles emerge with opposite azimuthal angle ϕ (assuming perfectly head-on e^+e^- collisions) and with correlated values of θ_{lab} as shown in the plots of Fig. 25. These correlations can be used to identify the events provided the emission angles are measured with sufficient accuracy. It can be seen that this method is more difficult at small $E_{c.m.}$ where small angular differences are involved. In fig. a the angular correlation for NNbar at two energies is compared with that for other two-body channels. NNbar is well separated from these other two-body reactions.

2. The velocity of the two particles in the laboratory system is significantly smaller than c in most of the region of interest, suggesting the use of time of flight to identify events and reject prompt photons and other fast backgrounds. In Fig. 27 the time difference between prompt photons and nucleons as a function of p is shown for a 1 m flight path.

In this respect a crucial parameter is the length of the flight path of the particles that determines linearly the discrimination power of the method. The plot shows that in order to have a difference larger than 1 ns over the full momentum spectrum, a flight path of at least 4 m is required. A difficulty for this method is the short inter-bunch time of $T_{b.c.} = 4.2\ ns$ that introduces a further free parameter-the bunch crossing time; for every event it must be found using all the information coming from the event.

3. In the case of $p\overline{p}$, momentum analysis of both particles allows identification of the event, since the sum of energies of the two particles must equal $E_1 + E_2$. Moreover the momenta of p and $\overline{p}$ are anticorrelated. Rejection of pions can be done by means of the dE/dx measurement described in the tracking section.

4. The interactions of 1 GeV nucleons and antinucleons with calorimeter materials allows in principle their distinction from electromagnetic showers based mainly on longitudinal shower profile.

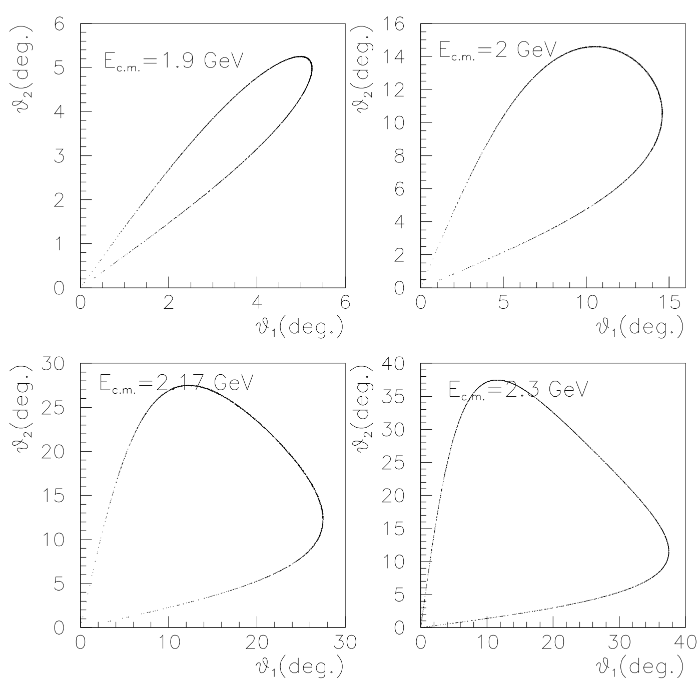

FIG. 25. Angular correlations between the two nucleons at four different center of mass energies. θ_1 and θ_2 are the polar angles of the nucleons in the laboratory system.

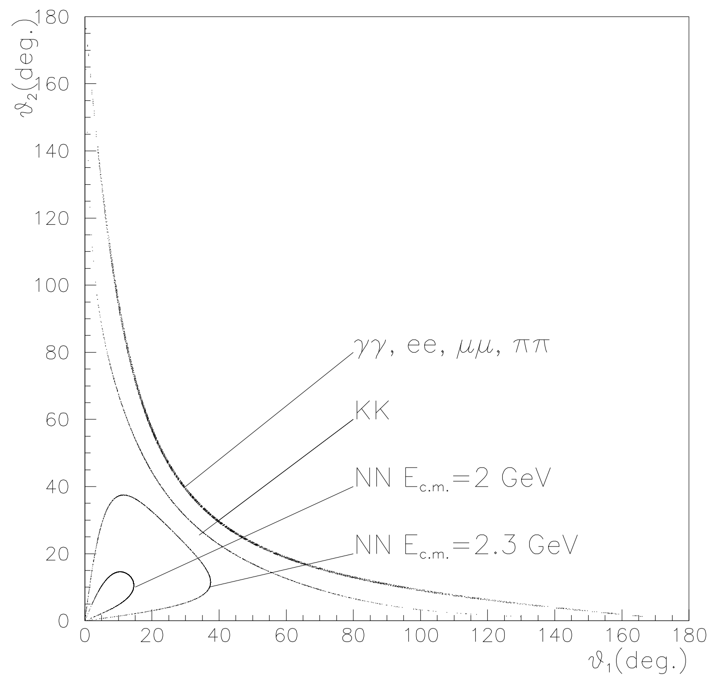

FIG. 26. Angular correlation in the center of mass system for two-body final states.

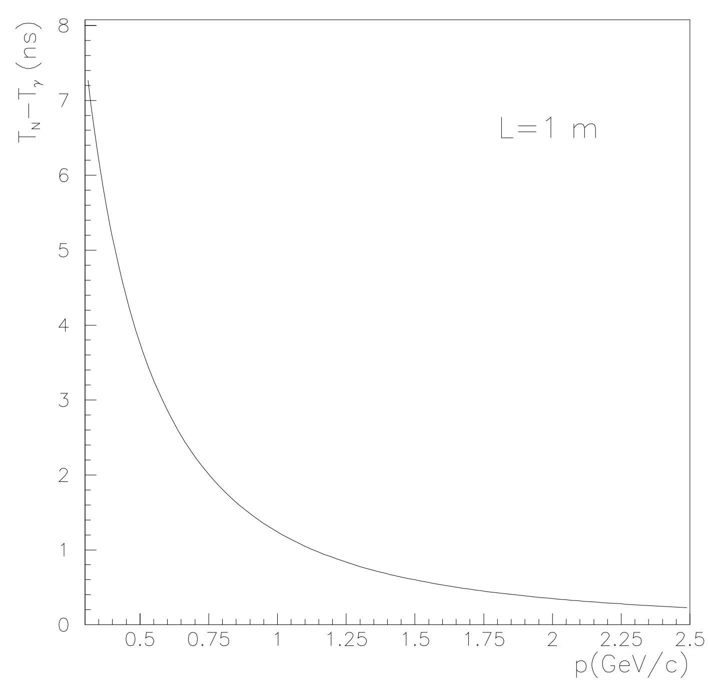

FIG. 27. Difference between the time of flight of a nucleon and that of a photon for a 1 m distance as a function of particle momentum.

b. Angular distribution

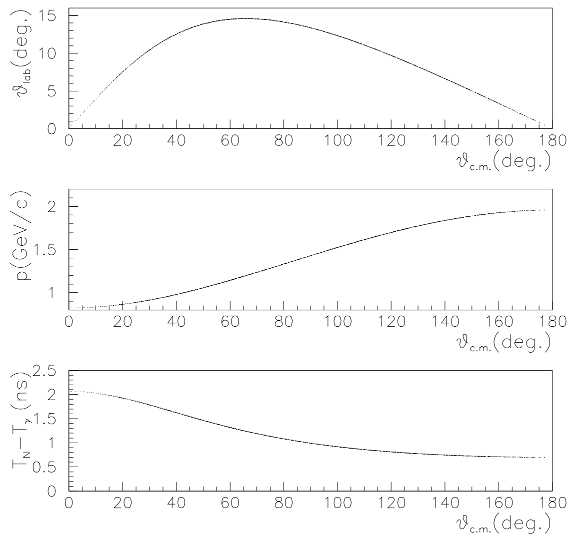

FIG. 28. Dependence of the laboratory angle, momentum, and time of flight for a 1 m flight path on the center of mass angle theta for a center of mass energy of 2 GeV.

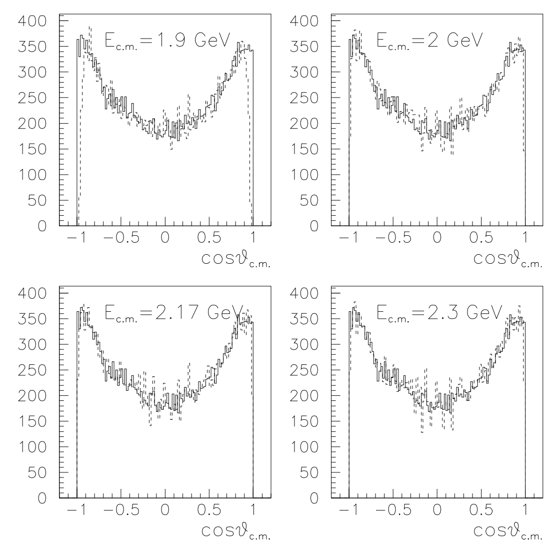

FIG. 29. Comparison between the generated(solid) and reconstructed by kimematical fitting (dashed) $cos\theta_{c.m.}$ distributions for four values of $E_{c.m.}$. A $1{+}cos^2\theta_{c.m.}$ distribution has been used corresponding to $G_E = 0$. The loss at angles close to $\theta_{c.m.} = \pm 180^o$ is due to the nucleons below 1^o. The loss is more significant at low $E_{c.m.}$ as expected.

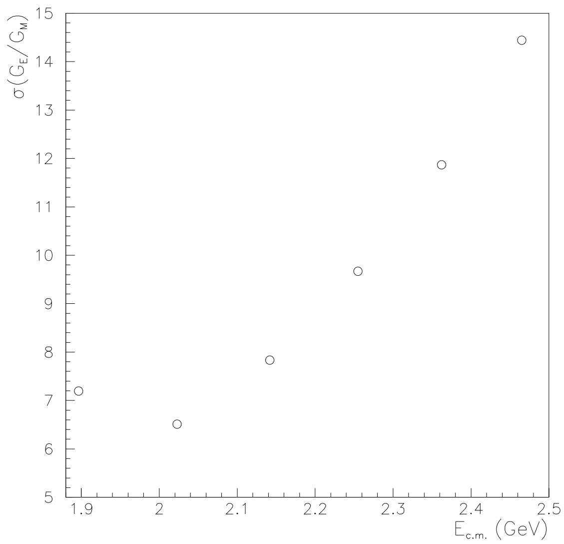

FIG. 30. Relative uncertainty in G_E/G_M as a function of $E_{c.m.}$ for 10 days of data taken at an average luminosity of 5×10^{30} with an efficiency of 50%. Only statistical uncertainty is considered.

An important goal of the experiment is determination of the center of mass angular distribution in order to separately evaluate G_E and G_M. This requires determination of $\theta_{c.m.}$ on an event by event basis. Given the boost, the value of $\theta_{c.m.}$ determines the energy in the laboratory system and hence the time of flight, and, with a two-fold ambiguity, the laboratory polar angle θ_{lab}. The relations between these variables in the laboratory system and $\theta_{c.m.}$ are shown in Fig. 28 for $E_{c.m.} = 2\ GeV$. The measurement of θ_{lab} of only one particle is not sufficient to evaluate $\theta_{c.m.}$. Further information is required, provided by time of flight measurement for the case of $n\overline{n}$ and/or momentum measurement in the case of $p\overline{p}$. Using both particles a over-constrained kinematic fit can be done.

In order to investigate the reconstruction $\theta_{c.m.}$ for $n\overline{n}$ final states using laboratory variables a simple Monte Carlo simulation has been done with the following assumptions: neutrons and antineutrons are detected with a calorimeter at 5 m from the interaction region with a spatial resolution of 3 cm, a time resolution of 250 ps and an acceptance extending from 1^o to 45^o. A kinematic fit is done for every event using time and spatial measurements of both particles in the laboratory system. The results in Fig. 29 show that the center of mass angular distribution is well reproduced at for $E_{c.m.}$ greater than 1.9 GeV.

From the $\theta_{c.m.}$ distribution, we can fit to G_E/G_M. The resulting uncertainty in G_E/G_M is essentially statistical. A simulation shows that an uncertainty below 10% is obtained for $E_{c.m.}$ between 1.9 and 2.2 GeV for 10 days of data taking at a luminosity of 5×10^{30} $cm^{-2}s^{-1}$ with an efficiency of 50%. Fig. 30 shows the relative uncertainty in G_E/G_M obtained in 10 days of data taking as a function of $E_{c.m.}$. Increasingly larger data taking times are required to get the same uncertainty for values of $E_{c.m.}$ greater than 2 GeV due to the decrease of the cross section.

c. Backgrounds At PEP-N, $N\bar{N}$ pairs can be made in the process $e^+Z \rightarrow e^+ZN\bar{N}$, where Z represents a heavy nucleus present in residual gas or in the beam pipe. The laboratory energy of the $N\bar{N}$ is then smaller than the 3.1 GeV energy of the LER, w hich is smaller than energy of the $N\bar{N}$ formed in annihilation by the PEP-N beam energy of $> 0.285 GeV$, the $N\bar{N}$ threshold. Even if the e^+ is not observed in the detector, kinematical measurements (angles, energies, momenta) makes it poss ible to clearly distinguish these processes. This is particularly true for formation of $p\bar{p}$ where the fit is 4 constraint and the interaction point is well measured. For $n\bar{n}$, a signature that includes n and $\bar{n}$ is highly overconstrain ed and background events are easily distinguished. A one-particle signature (e.g. $\bar{n}$ angles plus time of flight) is potentially vulnerable to background. Rates based on expected machine conditions are calculable.

V. EXPERIMENTAL DESIGN

We describe below several options for detector subsystems that may be suitable for the multihadronic and/or nucleon-antinucleon measurements.

A. Magnet

The magnetic field integral in the interaction region is determined by machine requirements to be 0.3 $T \cdot m$ at the maximum e^- beam energy of 500 MeV. This field can also be exploited by the experiment, to provide momentum measurements, which can be achieved by fitting a tracking system (TPC or drift chamber) inside the magnetic field volume. In order to provide a suitable acceptance this volume should be of adequate size, and should have a θ aperture of at least 50° at 500 MeV (see table IV B).

The magnet built for CERN experiment PS170, which is now at CERN and available for use, can be modified to fulfill the requirements of the experiment. It is a dipole magnet, with a gap of 0.4 m, designed to provide a maximum field of 1.47 T over a length of 1 m. The gap size can be increased to 1.8 m in order to include the PEP-II High-Energy Ring (HER) beam pipe, which is located 0.9 m below the Low-Energy Ring (LER), without the need to drill a hole in the magnet pole. In this configuration the maximum field achievable is 0.3 T, thus giving the required field integral of 0.3 $T \cdot m$.

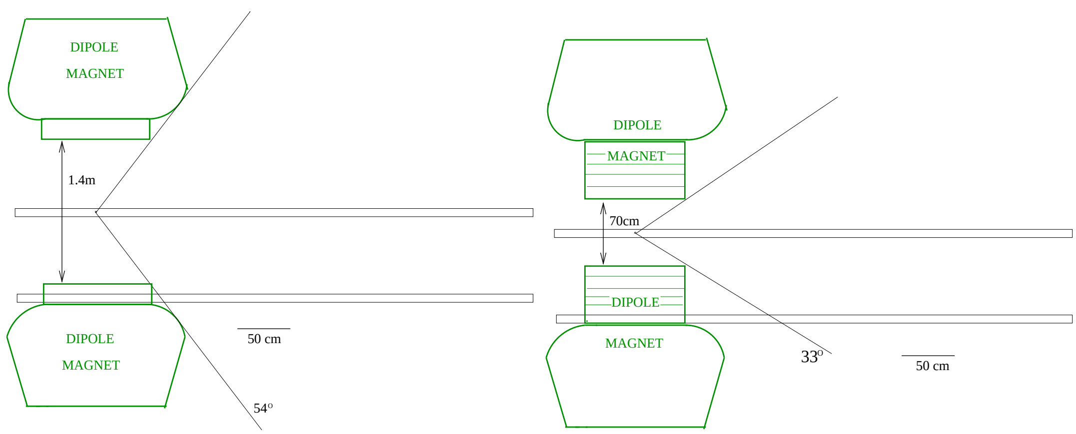

FIG. 31. Modified magnet configuration for PEPN

Exploiting the fact that the acceptance is not limited by the poles, but by the coils, the large fringe field which exists in the open configuration may be reduced by adding iron slabs to increase the pole size, as shown in Fig. 31 (a). One slabs can include the HER beam pipe, thus shielding it from the magnetic field if made of appropriate material. The gap would be reduced to 1.4 m, yielding the required field with a smaller current, while keeping the geometric acceptance the same. At lower energies, where a smaller acceptance is acceptable, the gap can be made even smaller by adding further slabs to the poles, as shown in Fig. 31 (b). This would further reduce the fringe field and the current required to achieve a given field. Alternatively, a higher maximum field could be achieved, up to 0.8 T.

B. Multihadronic detector

A possible detector for studying multihadronic final states is shown in figures 32 (side view) and 33 (top view). It consists of an inner tracking system inside the magnet described in the previous section and two calorimeters. The calorimeter system used in the Fermilab experiment E835, which is completing its last period of data taking, may be available for this experiment.

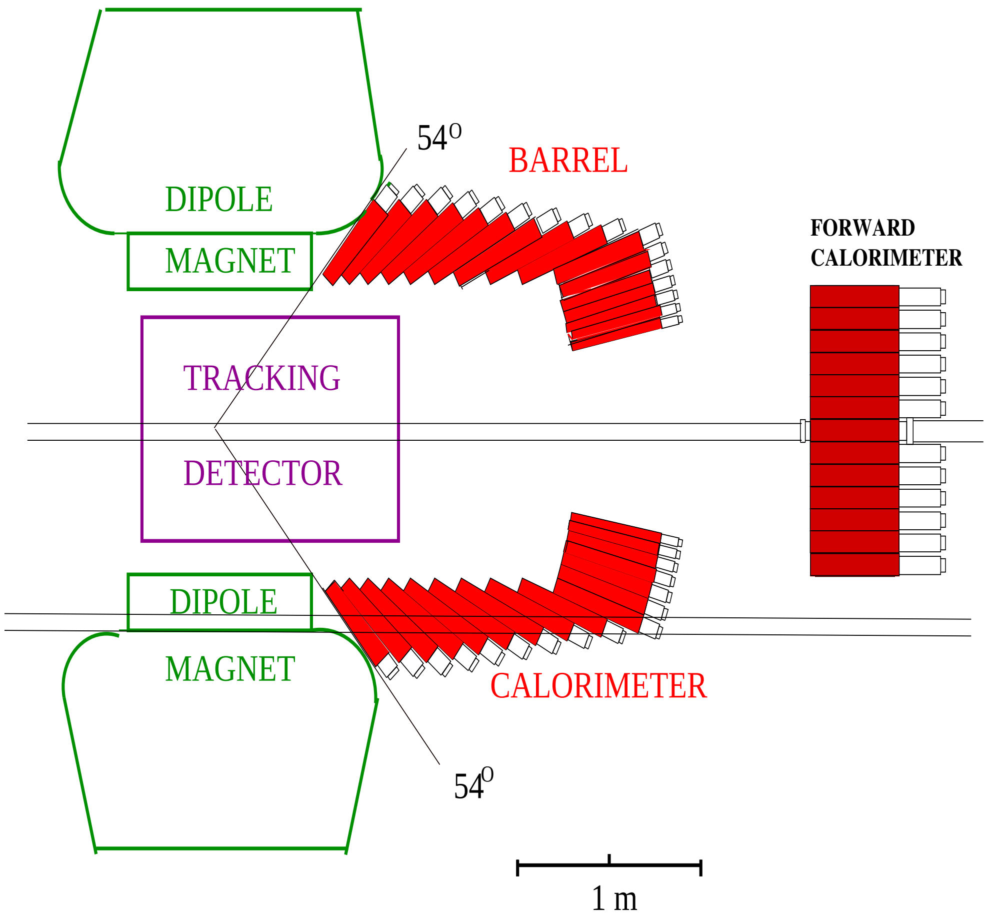

FIG. 32. Multihadronic detector - Side view

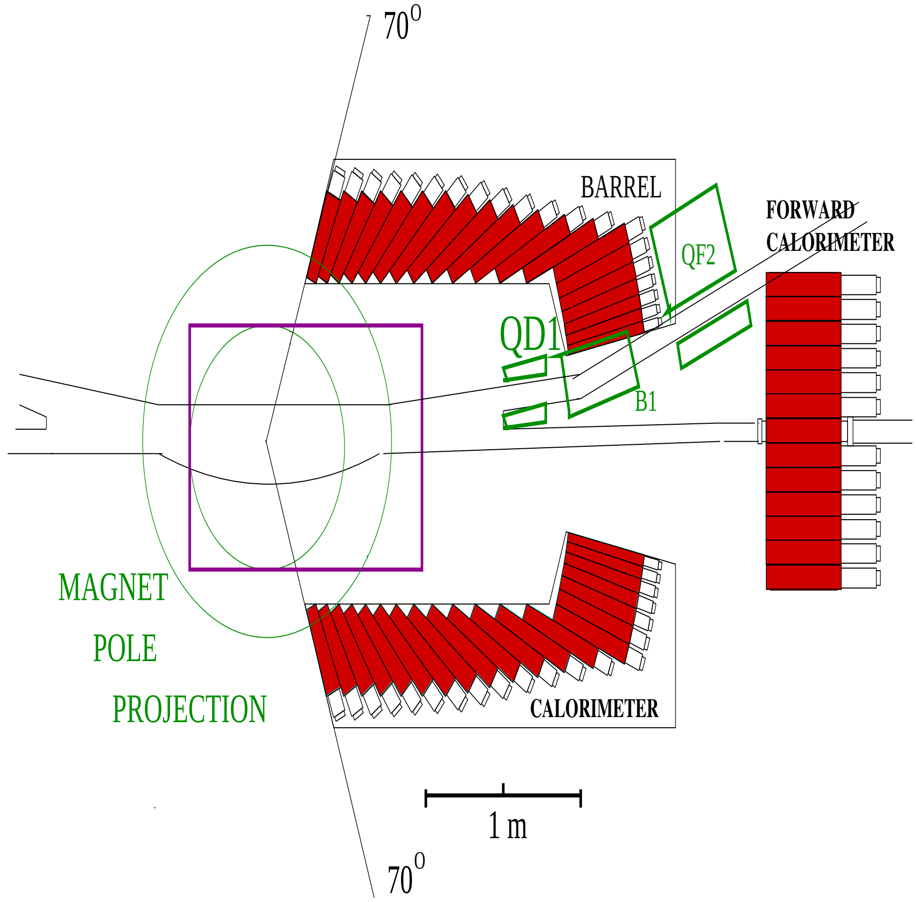

FIG. 33. Multihadronic detector - Top view

1. Inner tracking

The magnetic field region can be instrumented with a tracking system to allow momentum measurement, which is mainly useful for the multihadronic final states. The tracking system can consist of TPCs or drift chambers, with transverse dimensions compatible with the magnet gap, and longitudinal size of 0.5 m to 1 m.

The momentum resolution of this device is given by the spatial resolution of the tracking chambers and is limited by multiple scattering (m.s.). We assume a conservative single measurement resolution $\sigma = 150\ \mu m$, and evaluate the performance for 50, 25 and 10 measurements. The m.s. contribution is evaluated for a standard gas (argon) and for helium, as the results for argon are quite large. Results are reported in tables 2, 3 and

4, corresponding to track lengths of 1 m, 0.5 m and 0.25 m respectively. In each table the various contributions to the momentum resolution are reported for each energy (and corresponding value of B).

e^- energy (MeV)	B (T)	multiple scattering contribution		space resolution contribution		
		Ar	He	50 p	25 p	10 p
300	0.18	3.6 %	1.7 %	0.9 %	1.1 %	1.6 %
400	0.24	3.0 %	1.4 %	0.7 %	0.9 %	1.2 %
500	0.30	2.2 %	0.9 %	0.6 %	0.7 %	1.0 %

TABLE III. Momentum resolutions with 1 m track length.

e^- energy (MeV)	B (T)	multiple scattering contribution		space resolution contribution		
		Ar	He	50 p	25 p	10 p
300	0.18	5.3 %	2.2 %	3.3 %	4.4 %	6.3 %
400	0.24	4.2 %	1.8 %	2.5 %	3.4 %	4.8 %
500	0.30	3.3 %	1.7 %	2.1 %	2.8 %	4.0 %

TABLE IV. Momentum resolutions with 0.5 m track length.

e^- energy (MeV)	B (T)	multiple scattering contribution		space resolution contribution		
		Ar	He	50 p	25 p	10 p
300	0.18	7.2 %	3.2 %	13 %	18 %	25 %
400	0.24	5.7 %	2.6 %	10 %	14 %	19 %
500	0.30	4.6 %	2.0 %	8.3 %	11 %	16 %

TABLE V. Momentum resolutions with 0.25 m track length.

We observe that m.s. gives a significant contribution to the resolution, particularly for Ar; it can be reduced to approximately 2 % using He and a 1 m track length.

B (T)	multiple scattering contribution		space resolution contribution		
	Ar	He	50 p	25 p	10 p
0.4	1.8 %	0.7 %	0.5 %	0.5 %	0.6 %
0.5	1.7 %	0.6 %	0.5 %	0.5 %	0.5 %
0.6	1.0 %	0.6 %	0.5 %	0.5 %	0.5 %

TABLE VI. Momentum resolutions with 1 m, E=500 MeV

In table 5 we report the m.s. and chamber resolution contributions to the momentum resolution for higher values of the magnetic field and a 1 m track length at 500 MeV. We see that for a higher magnetic field the momentum resolution can be further improved to approximately 1%.

The above calculation shows that a 1 m chamber filled with Helium with as few as 10 measurements along each track will provide adequate momentum resolution. The total number of measurements along each track will be chosen to obtain the dE/dx resolution required to achieve good $\pi - K$ separation.

2. Calorimeter

In its present setup the central calorimeter [65] (CCAL) is a matrix of 1280 lead glass counters (64 in ϕ by 20 in θ) pointing to the interaction region, measuring the energy and direction of electrons and photons. The CCAL has an energy resolution $\sigma_E/E = 0.014 + 0.06/\sqrt{E(\mathrm{GeV})}$ and an angular resolution (r.m.s.) of 11 mrad in ϕ and 6 mrad in θ; these angular errors include the contribution of the finite size of the interaction region, which in E835 is approximately 6 mm in both the transverse and longitudinal directions. Each counter in CCAL is equipped with an ADC to measure pulse height and a TDC to provide timing information to reject pile-up. All showers with energy above 80 MeV can be identified as 'in time' or 'out of time'. Showers with lower energy sometimes have no TDC information and are then labeled 'undetermined'. The CCAL energy threshold is 20 MeV.

The pointing geometry of this detector can be preserved for our experiment with the configuration shown in figures 32 and 33. In the region of the coils (where the acceptance is limited to $\theta \leq 54°$) a few blocks in the 4 rings at high θ must be removed. In addition, a few blocks must be removed to make room for the HER and VLER beam pipes and bending magnets QD1, B1 and QF2.

The region at low θ can be instrumented with a forward calorimeter (FCAL), also in use by Fermilab E835. It is a matrix of 144 lead-glass blocks covering $3.5° \leq \theta \leq 10°$. It has an energy resolution $\sigma_E/E = 0.12/\sqrt{E(\mathrm{GeV})}$, and a position resolution $\sigma_{x,y} = 6\ cm$, corresponding to an angular resolution of approximately 20 mrad in the setup of figures 32 and 33.

C. Nucleon antinucleon detector

The $N\overline{N}$ detector is expected to cover the forward angular region from $\sim 1^o$ with respect to the beam line up to at least 45^o. It has to provide detection of n, $\overline{n}$, p and $\overline{p}$ in the momentum range from 0.3 up to 2.5 GeV/c with good efficiency. Measurement of time of flight and of flight direction is required for all these particles. In the case of p and $\overline{p}$ momentum analysis can be useful. Furthermore this detector is used also to detect the forward charged and neutral particles of the multihadronic events escaping the main multihadronic detector.

A sequence of a tracking device and a calorimeter seems suitable. The tracking device has to identify p and $\overline{p}$, measure directions and if inside a magnetic field measure momenta; the calorimeter should be efficient for neutrons, allow the antineutrons to interact, and should provide time of flight and impact position of both neutral particles. detector in side view.

The distance L along the beam line between the face of the detector and the interaction region can be any value between about 1 and 5 meters. A minimum distance R from the beam line of about 10 cm is imposed by the size of the beam pipe. The larger the distance L the better is the time of flight and angular discrimination power, and the smaller the acceptance loss at small angles due to the beam pipe. On the other hand the smaller the distance, the larger is the angular acceptance for a given detector size. The possibility of mounting the detector on a moveable platform in orderto change its distance from the interaction region depending on $E_{c.m.}$ is being considered.

Here we show two possible options under study.

1. In the first configuration (shown in Fig. 34) the detector is close to the interaction region and consists of a tracking section out of the magnetic field and of a calorimeter covering the full angular region. The smaller distance to the interaction region allows

extending the angular range to 33^o in the side projection and to 54^o in the top projection with a single detector, but is limited at small angles where the size of the beam pipe implies a minimum of $\sim 5^o$.

2. In the second configuration (shown in Fig. 35), the $N\overline{N}$ detector consists of a tracking section at about 4.5 m from the interaction region, a calorimeter at the maximum allowed distance of 5 m, covering the low θ_{lab} region between 1.2^o and 17^o and two smaller calorimeters closer to the interaction region to cover larger values of θ_{lab} up to about 45^o.

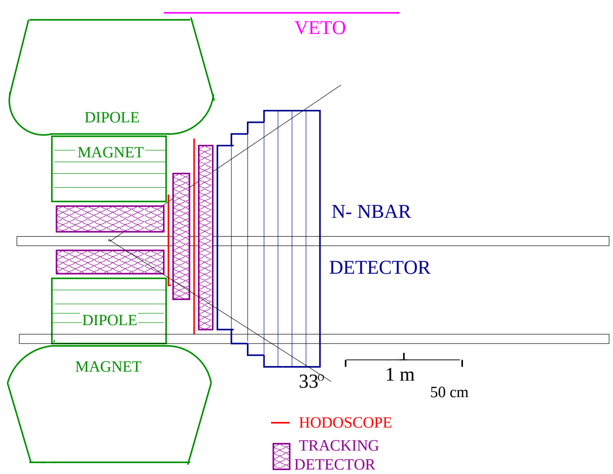

FIG. 34. Schematic view of the $N\overline{N}$ detector (first option).

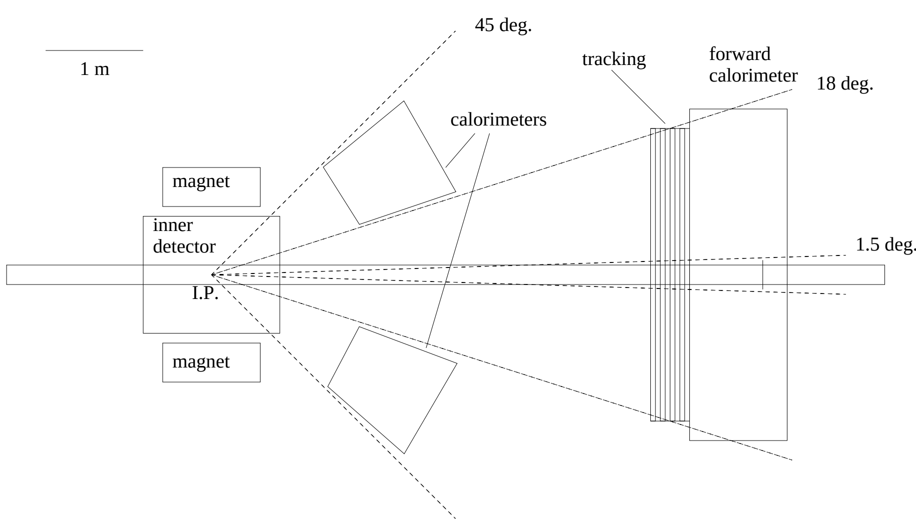

FIG. 35. Schematic view of the $N\overline{N}$ detector (second option).

1. *Tracking section*

The tracking section provides discrimination between charged and neutral particles, and provides a precision measurement of the flight direction for p and $\overline{p}$. It must be nearly transparent for n and $\overline{n}$ to let them interact in the calorimeter. Chambers, drift tubes, RPCs and streamer tubes are all possible options. If the tracker is within the magnet it will provide momentum analysis.

2. *Calorimeter section*

We consider plastic scintillation counters with or without lead or iron absorbers. Further trackers can be inserted between the layers of plastic scintillator to allow tracking of the products of $\overline{n}$ annihilation and improve particle identification.

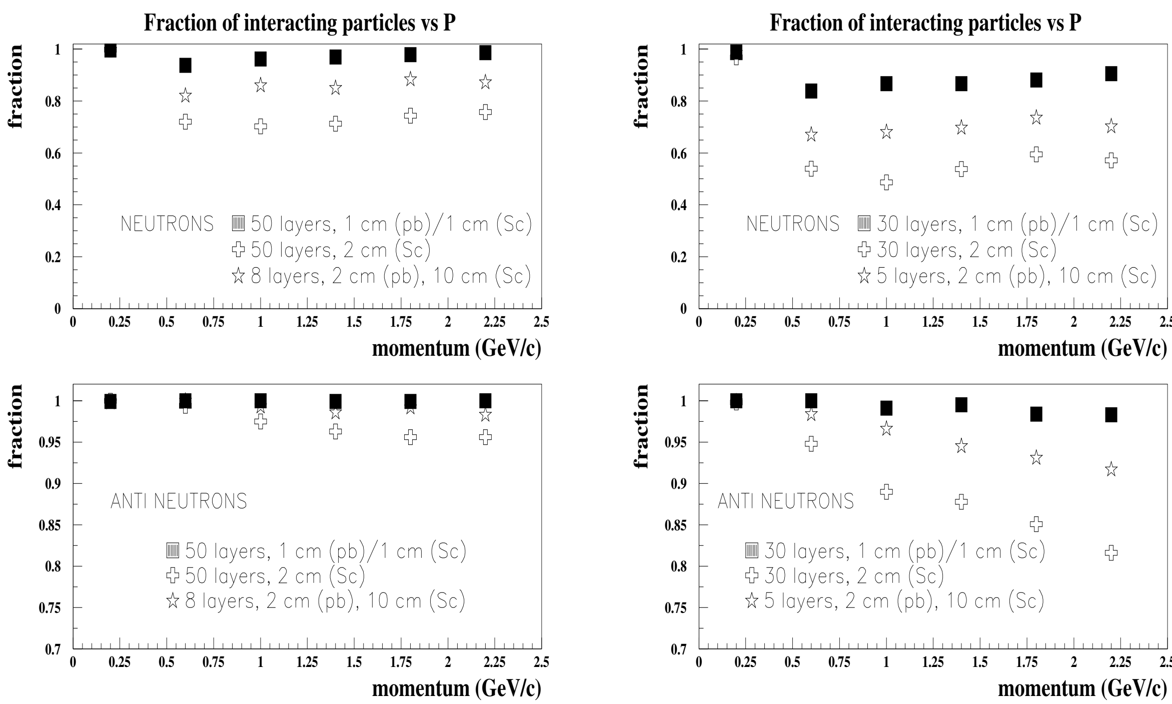

FIG. 36. Probability of interaction for neutrons and antineutrons in the simulated calorimeter structure as a function of the particle momentum. 1 m thick calorimeters (configurations C1a, C2a and C3a) are shown in the upper plots, thinner calorimeters (configurations C1b, C2b and C3b (60 cm)) in the lower plots.

The efficiency for neutrons and antineutrons has been studied with a GEANT Monte Carlo simulation of lead-scintillator structures in the following configurations:

C1 : 1cm Pb + 1cm Scint. (a) 50 layers (b) 30 layers

C2 : 2cm Pb + 10cm Scint (a) 8 layers (b) 5 layers

C3 : only scintillator (a) 1 m thick (b) 60 cm thick

Option C2 is motivated by the possibility of using scintillator bars $10 \times 10 \times 160 cm^3$ equipped with photomultipliers at both ends available from another experiment [66]. Options (a) correspond to an overall thickness of 1 m, options (b) of 60 cm.

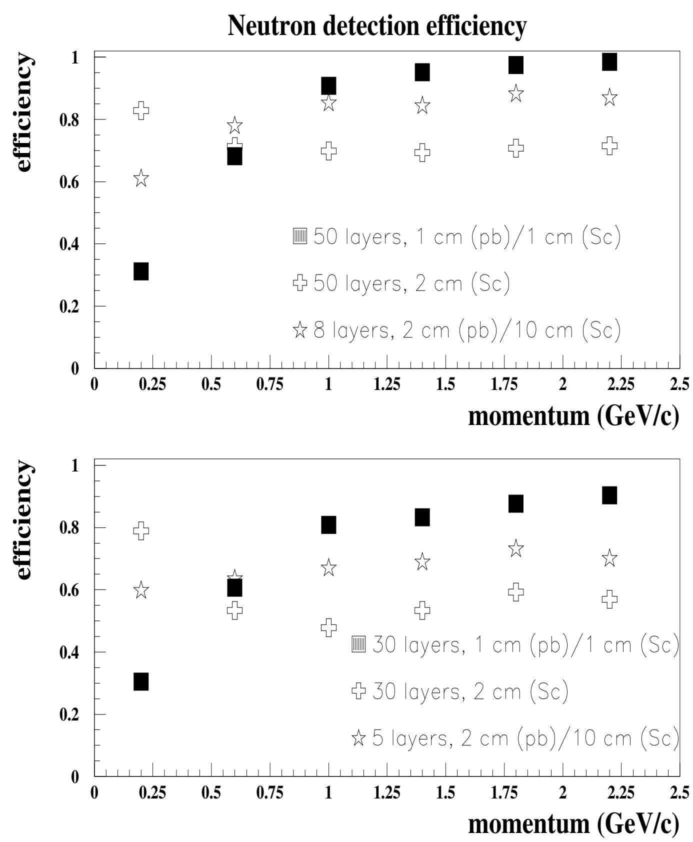

FIG. 37. Efficiency for neutron detection as a function of neutron momentum for the considered calorimeter configurations.

Fig. 36 shows the probabilities of interaction for neutrons and antineutrons as a function of the particle momentum for the different configurations. The probability of interaction depends mainly on the mass of material. All of the configurations give an antineutron interaction probability larger than 80 %; smaller (but larger that 50 %) interaction probabilities are found for the neutron.

Results for the neutron efficiency are shown in Fig. 37. The detector is considered efficient when at least 4 MeV of energy is deposited in one scintillator layer. For momenta larger than 1 GeV/c the efficiency approaches the probability of interaction (compare with Fig. 36). For smaller momenta, the probability that the energy deposited in the scintillator by the interaction is below the fixed threshold becomes relevant, and depends mainly on the fraction of inert material. The drop in efficiency at low momenta is essentially due to neutron interactions where the proton does not escape from the lead (or iron). The configuration without lead gives a smaller but less energy-dependent efficiency.

Fig. 38 shows an example of a $n\overline{n}$ Monte Carlo event in configuration 1.

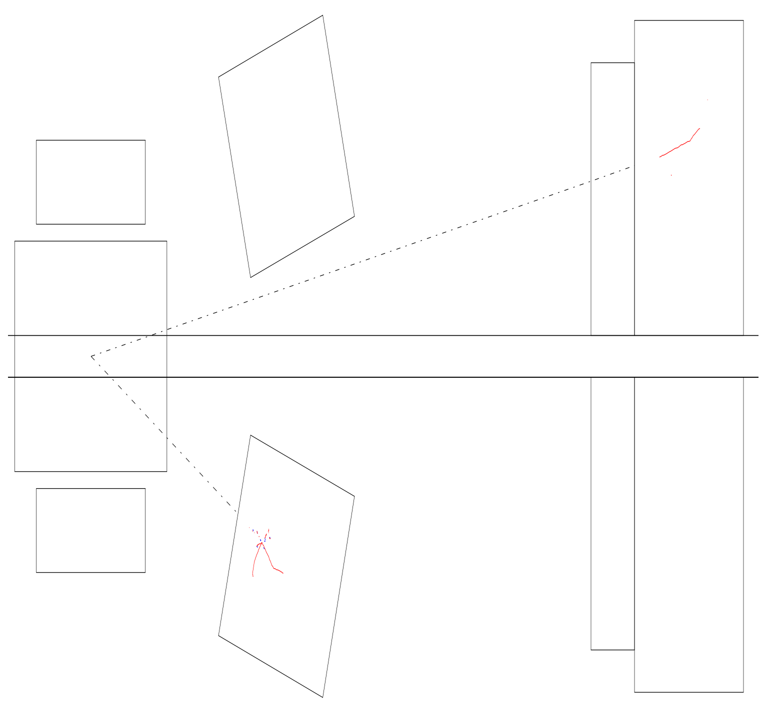

FIG. 38. Example of $n\overline{n}$ event for $E_{c.m.} = 2.2\ GeV$ with $N\overline{N}$ detector option 1 and calorimeter structure 1a. The particle at lower angle is the neutron.

D. Conclusion

We have shown that it is possible to build a detector capable of performing the proposed measurements, at a reasonable cost affordable by the collaboration and compatible with the accelerator in its present design. The final choice of technologies, materials etc. will be made when all details of the accelerator are fixed and will be particularly dependent upon the magnetic field requirement for the interaction region.

Appendix I

Nucleon timelike form factors

For $e^+e^- \to N\overline{N}$ the differential cross section in the c.m. is given by [67]:

$$\frac{d\sigma}{d\Omega} = \frac{\alpha^2\beta C}{4s}\Bigg[(1-P_LP_L')\left(|G_M(s)|^2(1+\cos^2\theta)+\frac{4M_N^2}{s}|G_E(s)|^2\sin^2\theta\right) + P_TP_T'\left(|G_M(s)|^2-\frac{4M_N^2}{s}|G_E(s)|^2\right)\sin^2\theta cos2\phi\Bigg] \quad (5)$$

where β is the nucleon velocity in the c.m., s is the c.m. total energy squared, $G_M(s)$ and $G_E(s)$ are the magnetic and electric form factors, respectively , expected to be the analytical continuation of the spacelike form factors $G_E(Q^2)$ and $G_M(Q^2)$. P_L and P_L' are respectively the longitudinal polarizations of the electron and positron and P_T and P_T' are the respective polarizations perpendicular to the storage ring plane. $G_E(0)$ is 1 for the proton and 0 for the neutron and $G_M(0)$ is 2.79 for the proton and -1.91 for the neutron, giving the static charge and magnetic moment of the nucleons. For the proton, $C \sim \frac{\pi\alpha}{\beta}/(1-e^{-\pi\alpha/\beta})$ is a Coulomb correction significant at very small nucleon kinetic energy and makes the cross section at threshold non-zero; $\sigma_p(4M_N^2) \simeq \pi^2\alpha^3|G_E|^2/(2M_N^2)$. Assuming that the Dirac form factor, $F_1 = (G_E - \frac{s}{4M_N^2}G_M)/(1-\frac{s}{4M_N^2})$, and the Pauli form factor, $F_2 = (G_M - G_E)/(1-\frac{s}{4M_N^2})$, are analytical through the $N\overline{N}$ threshold, we have $G_M(4M_N^2) = G_E(4M_N^2)$, i.e. exactly at threshold only S wave is present and the angular distribution is isotropic. At very high s the contribution from G_E is reduced by the helicity factor $4M^2/s$.

The proposed experiment at PEP-N anticipates separately obtaining G_E and G_M by studying the angular distribution given above. Most prior experiments in the timelike regime, with limited statistics and limited angular acceptance, were not able to separate G_E and G_M and data were analyzed to obtain $|G_M|$ only, using the scaling *ansatz* $|G_E| = |G_M|$ at all values of s. Experiment PS170 (LEAR) made an effort to separate G_E and G_M and with relatively large uncertainties report that $|G_E|/|G_M|$ falls with increasing (timelike) $|Q^2|$, contrary to *form factor scaling.* Recent TJNAF data [68] shows that in the spacelike regime the ratio $|G_E|/|G_M|$ also falls with increasing $|Q^2|$. These data suggest that in the timelike regime, $|G_E|/|G_M|$ may fall by as much as 30% as $\sqrt{s}$ increases from threshold to $\sim$ 6.25 GeV^2.

If transversely polarized colliding beams are available, additional power to separate $|G_E|$ and $|G_M|$ is obtained by studying the ϕ distribution of the differential cross section.

The cross sections for $e^+e^- \to N\overline{N}$ are roughly comparable; each is $\sim$ 1 nb at a $\sqrt{s}$ of 2 GeV.

Appendix II

Meson timelike form factors

For $e^+e^- \to \pi^+\pi^-$, the differential cross section in the c.m. is given by:

$$\frac{d\sigma}{d\Omega} = \frac{\alpha^2\beta^3}{8s}\left[|F_\pi(s)|^2 \sin^2\theta\right] \tag{6}$$

where F_π is the pion form factor which is again the analytical continuation of the spacelike form factor and $F_\pi(0) = 1$ A similar expression describes $e^+e^- \to K^+K^-$ where the kaon form factor is $F_K(s)$ and $F_K(0) = 1$. For $e^+e^- \to K^0\bar{K}^0$ we again have the same expression where $F_{K_0}(0) = 0$.

The reaction $e^+e^- \to V^+V^-$ where V is the ρ or K^* is not consistently described in QED, reflecting the well-known problem with renormalization in spin-one electrodynamics. One can describe the cross section either in terms of s-dependent helicity amplitudes that are coefficients of the following terms in the differential cross section: $sin^2\theta$, $(1 + cos\theta)^2$ and $(1 - cos\theta)^2$, or in terms of charge, magnetic moment and quadrupole moment form factors. Renard [67] gives the differential cross section for the formation of vector meson pair for the general case of polarized beams in terms of the latter. In either description the parameters are determined by the quark wave function of the vector meson in question.

The cross section for $e^+e^- \to \pi^+\pi^-$ at a $\sqrt{s}$ of 2 GeV based on existing data is ~ 0.5 nb and that for $e^+e^- \to K^+K^-$ is comparable. The cross section for annihilation to pairs of vector mesons is also expected to be roughly comparable as their wave functions are spatially similar to those of the vector mesons.

Appendix III

Form factors via initial state radiation at BABAR

We examine the possibilities for studying form factors in the low energy regime at BABAR, using events with hard initial state radiation, i.e. $e^+e^- \to \gamma + f$.

The rate of such events in the center of mass interval ΔW, $\dot{n}$, is :

$$\dot{n} \sim L_{PEP-II} \cdot \sigma_W(e^+e^- \to f) \cdot \beta \frac{\Delta k}{k}[1 - \frac{2k}{W_0} + \frac{2k^2}{W_0^2}] \cdot \epsilon_{BABAR}$$

where:

- $W = \sqrt{W_0^2 - 2kW_0}$ is the c.m. energy after a photon of energy k has been emitted (W_0 is the PEP-II c.m. energy),
- $\sigma_W(e^+e^- \to f)$ is the cross section for a final state f at a c.m. energy W,
- $\beta = \frac{4\alpha}{\pi}[log(\frac{W}{m_e}) - 0.5] \sim$ 0.083 is the Bond factor,
- $\Delta k = -\frac{W}{W_0} \cdot \Delta W$ is the radiative photon energy range corresponding to the c.m. energy interval ΔW,
- ϵ_{BABAR} is the BABAR detection efficiency for this kind of events.

The PEP-II asymmetric configuration and the forward and backward BABAR acceptance are such that the detection efficiency is much higher in case of initial state radiation emitted by the high energy beam [69] [70] [71]. In this case the boost of the hadronic final state, because of the photon emission, is opposite to the PEP-II boost ($\beta_{PEP-II} = 0.49$) and it is, in the lab, $\beta_f = -0.81$ at $W = 2GeV$ and $\beta_f = -0.62$ at $W = 3\ GeV$.

For most of the reactions of interest it is necessary to detect the initial state radiative photon to suppress backgrounds from $\gamma\gamma$ interactions. The BABAR angular acceptance for these photons is $p_\gamma \sim 10\ \%$.

The BABAR effective luminosity L_{eff} for these events is then

$$L_{eff} \sim L_{PEP-II} \cdot \beta \frac{\Delta k}{k}[1 - \frac{2k}{W_0} + \frac{2k^2}{W_0^2}] \cdot \frac{1}{2} \cdot p_\gamma \ \sim \ 3.5 \cdot 10^{28}\ cm^{-2} s^{-1}$$

where we take $L_{PEP-II} \sim 3 \cdot 10^{33} cm^{-2} s^{-1}$ and $\Delta W \sim 100\ MeV$. We do not consider the BABAR efficiency ϵ_{BABAR}, which varies by reaction, in this estimate.

The final state $p\overline{p}$ is considered first. Detection of the radiative photon may not be required for this simple topology as it may be possible to reject backgrounds by requiring equality of the forward missing energy and missing momentum, thanks to the very good DCH momentum resolution. To identify a several GeV $p\overline{p}$ pair the DIRC and several layers of the DCH must be hit. Therefore a minimum opening angle of the $p\overline{p}$ pair is required, which we estimate to be $\pm 30^o$ at least, corresponding to a minimum $p\overline{p}$ invariant mass $M_{p\overline{p}} \geq 2.4\ GeV$. For higher $M_{p\overline{p}}$ the minimum opening angle corresponds to a cut in the $p\overline{p}$ c.m. angle θ^*. For $M_{p\overline{p}} \sim 3\ GeV$ we have $|cos(\theta^*)| \leq 0.4$, which precludes separation of the electric and magnetic form factors.

The expected number of events $N_{p\overline{p}}$ in the center of mass energy interval $2.4 \div 3.0\ GeV$ is no greater than 100- 200. Here we do not require that the radiative photon be detected, take a PEP-II integrated luminosity of 100 fb^{-1} and cross sections of $\sim 70\ pb$ at 2.4 GeV, as measured by DM2 [31], and $\sim 6\ pb$ at 3 GeV, as measured by E835 [31] at FNAL by means of $p\overline{p} \rightarrow e^+e^-$.

A much smaller number of identified $n\overline{n}$ events is expected. In this case the radiative photon must be detected, due to the absence of a neutron (antineutron) momentum measurement, and the overall BABAR detection efficiency for a several GeV $n\overline{n}$ pair is less than $\sim 10\ \%$ [71].

The prospect for an R measurement has not yet been studied. For such a measurement the radiative photon must certainly be detected to suppress $\gamma\gamma$ multihadronic events. The BABAR backward angular acceptance is about $\sim 50\ \%$ for a relativistic particle with an isotropic c.m. distribution and with the aforementioned boost along the beam.

Appendix IV

University of Virginia Neutron Detector

The University of Virginia neutron detector consists of 79 plastic scintillator bars 1.6m by 10 cm by 10 cm complete with light pipes and phototubes at each end. The bars, for neutron detection, have been typically arranged in a vertical stack consisting of multiple layers. The rejection of charged particles is provided by 39 thin plastic paddles 1.6m by 11cm by 1 cm, also with light pipes, PMTs and bases arrangned so as to precede the bars and provide the same solid angle coverage. The performance of these elements is well understood. They have been most recently used at Jefferson Lab in an experiment measuring the electric form factor of the neutron, G_e^n, through $\vec{D}(\vec{e}.en)p$ at a $Q^2 = 0.5(GeV/c)^2$. The average value of the kinetic energy of the neutron in this experiment was 267 MeV.

The scintillator material is Bicron 408 which has a bulk attenuation length of 380 cm, an index of refraction of 1.58, and a density of 1.03 g/cm^3. The system was designed to serve as TOF counter in which the energy resolution of the detected particles is given by

$$\frac{\Delta E}{E} \approx \gamma(\gamma+1)((\frac{\Delta l}{l})^2 + (\frac{\Delta t}{t})^2)^{\frac{1}{2}}$$

thus requiring the measurement of the flight time of the particle and the event position in the detector. The quadrature sum of the intrinsic time resolution of the detector with the timing signal is given by Δt and Δl is the uncertainty in the particle flight path due to the finite detector thickness (and any target thickness). The time resolution determined in the recent experiment at JLAB[1] was determined from the time of flight peak of the gamma flash in the meantime spectrum and was found to be 450 ps (σ). This gave a energy resolution of 16.5 MeV with the detector positioned 4 meters from the target. The intrinsic timing resolution of the bars themselves was measured in a bench test prior to the experiment using cosmics and was found to be 196 ns. Combined with the 100 ns timing resolution of the timing

[1] E93-026, A Measurement of the Electric Form Factor of the Neutron

signal the overall time resolution was expected to be 297 ps. Thus the experimental result was not as good as expected. This is under investigation. The effective light propagation velocity was detemined to be 14.3 cm/ns and the position resolution was found to be 5.9 cm.

At JLAB the detector was housed in a concrete shielded hut open to the target and was positioned 4 meters from the target. The layout of the elements was determined in an attempt to maximize the figure of merit for detection of the neutrons detected in coincidence with electrons scattered quasielastically into the eelctron spectrometer. The single plane of thin paddles and bars that extend above the bulk of the detector wer to allow for detecton of the quasielastically scattered protons that were bent vertically by the polarized target magnetic field.

Particle identification was achieved primarily by use of the information from the veto detectors and by the hit pattern in the bars. Photons were distinguished from charged particles by timing information. The veto inefficiency per plane was determined to be about 3.5% at our nominal beam current. With two veto planes, the overall veto inefficiency was roughly 0.12%.

Tracking was determined from the hit pattern in the bars that typically had only one hit per event. If the meantime of the hit fell within a tight window in the meantime spectra and there were no hits in the veto detectors the event was assumed to originate at the target and to be a neutron. An ADC cut was made to eliminate the hits due to the low energy background.

The neutron detecion efficiency is a function of neutron energy and detector threshold. No absolute measurement of the efficiency was made during the experiment. However, Monte Carlo calculations indidcate that the neutron detection efficiency is approximately 1% per cm and falls with increasing threshold and with increasing neutron energy. The rates during the experiment were compared with the results of a Monte Carlo. The Monte Carlo included the detector efficiency (corresponding to our discriminator threshold) and accounted for the loss of flux at each detector plane. The comparison between the experimental rates and the simulaton where found to be in reasonable agreement if an overall normalization of 0.75 was applied to the simulation.

It was necessary to shield the detector from low energy particles in order to reduce the rates in the first bar planes. A total of 16.7mm of lead and 25.4 mm of CH_2 absorber were positioned between the target and the face of the detector.

We follow with efficiency vs. threshold calculations for the range of neutron energies relevent, obtained using code written at Kent State University by Madey et al. [NIM 161 (1979) 439-447]. Efficiencies are shown for various thresholds between one and forty MeV (electron equivalent). These calculations are done for a neutron bar measuring 10 cm x 10 cm x 160 cm.

Energy (MeV)	e(%) @ 1	e(%) @ 5	e(%) @ 10	e(%) @ 15	e(%) @ 20	e(%) @ 25	e(%) @ 40
267	11.3	10.2	9.4	8.6	7.8	7.1	5.0
533	11.4	10.2	9.2	8.3	7.3	6.4	3.9
799	11.3	10.0	8.9	7.7	6.6	5.6	3.4
1065	10.9	9.6	8.2	7.0	5.9	4.9	3.0

References

[1] A. D. Martin, J. Outhwaite and M. G. Ryskin, J. Phys. G**26**(2000) 600.

[2] Z. Kunszt hep-ph/0003057.

[3] M. Davier and A. Hocker, hep-ph/9805470.

[4] S. Groote *et. al.* Phys. Lett B**440** (1998) 375.

[5] S. Eidelman, F. Jegerlehner, A. L. Kataev and O. Veretin, Phys. Lett B**454** (1999) 369; F. Jegerlehner, hep-ph/9901386.

[6] M. Swartz, Phys. Rev. D**53** (1996) 5268, hep-ph/9509248.

[7] B. Pietrzyk, presented in the parallel session talk (PA-05e) at ICHEP 2000, Osaka, 27 July-2 Aug., 2000.

[8] A. D. Martin, J. Outhwaite and M. G. Ryskin, hep-ph/0008078.

[9] R. R. Akhmetshin *et. al.* (CMD-2 Collaboration), hep-ex/9904027.

[10] M. N. Achasov *et. al.* (SND Collaboration), hep-ex/9910057; Phys. Lett. b**462** (1999) 365.

[11] J. Z. Bai *et. al.* (BES collaboration), Phys. Rev. Lett. **84** (2000) 594.

[12] BES-II collaboration, presented in the parallel session talk (PA-05e) by Z. Zhao at ICHEP 2000, Osaka, 27 July-2 Aug., 2000.

[13] A. Gurtu, presented at ICHEP 2000, Osaka, 27 July-2 Aug., 2000.

[14] LEP Electroweak Working Group, CERN-EP-2000-016, page 46.

[15] V. W. Hughes and T. Kinoshita, RMP **71** (1999) S133.

[16] H. N. Brown *et. al.* hep-ex/0009029, to be published in Phys. ReV. D62, Rapid Communica-

tions.

[17] M. Gourdin and E. de Rafael, Nucl. Phys. B**10** (1969) 667.

[18] S. J. Brodsky, G. PĿepage, Phys.Lett. 87B (1979) 359; A. Duncan, A. M. Mueller, Phys.ReV. D21 (1980) 1636.

[19] S. J. Brodsky, G. P. Lepage, Phys.Rev. D22 (1980) 2157;

[20] A. Antonelli et al, Phys.Lett. B313 (1993) 283; A. Antonelli et al., Nucl.Phys. B517 (1998) 3.

[21] H. W. Hammer, U. G. Meißner, D. Drechsel, Phys.Lett. B385 (1996) 343.

[22] U. G. Meißner, Nucl.Phys. A623 (1997) 340.

[23] V. Chernyak, A. Zhitnitsky, Nucl.Phys. B246 (1984) 52.

[24] H. N. Li, G. Sterman, Nuc. Phys. **B381**(1992) 129-140; N. Isgur, C. H. Llewellyn-Smith, Nuc. Phys. **B317**(1989) 526-572; P. Kroll et al., Phys. Lett. **B316** (1993) 546-554.

[25] A. A. Logunov, N. Van Hieu,I. Todorov, Ann.Phys. (NY) 31 (1965) v203.

[26] D. Bisello et al., Nucl.Phys. B224 (1983) 379, LAL 88-58 (1988).

[27] M. E. Biagini, L. Cugusi, E. Pasqualucci, Z.Phys. C52 (1991) 631.

[28] R. Gatto, N. Cabibbo, Phys.Rev. 124 (1961) 1577; J. C. Körner, M. Kuroda, Phys.Rev. D16 (1977) 2165; M. Giannini, E. Santopinto, M. Krivoruchenko, Dubna, 1994; S. Dubnička, Nuovo Cimento A104 (1991) 1075; A. Z. Dubničkova et al., Z.Phys. C70 (1996) 473.

[29] J. Ellis, M. Karliner, H. Kowalski, Phys.Lett. B235 (1990) 341; G. Holzwarth, Z.Phys. A356 (1996) 339.

[30] G. Bardin et al., Nucl.Phys. B411 (1994) 3.

[31] G. Bassompierre et al., Phys.Lett. B68 (1977) 477; B. Delcour et al., Phys.Lett. B86 (1979) 395; D. Bisello et al., Z.Phys. C48 (1990) 23; T. A. Armstrong et al., Phys.Rev.Lett. 70 (1992)

1212; A. Antonelli et al, Phys.Lett. B334 (1994) 431; E835 coll. M. Ambrogiani et al., PR D60 (1999) 32002.

[32] V. A. Matveev, R. M. Muradyan, A. N. Tavkhelidze, Lett.Nuovo Cim. 7,15 (1973) 719; S. J. Brodsky, G. R. Farrar, Phys.Rev.Lett. 31 (1973) 1153.

[33] T. Gousset, B. Pire, Phys.Rev. D51 (1995) 15.

[34] A. Antonelli et al, Phys.Lett. B365 (1996) 427.

[35] P. J. Franzini, F. J. Gilman, Phys.Rev. D32 (1985) 237.

[36] C. B. Dover, Proc. 4th Int.Symp. on $N\overline{N}$ Int.,Syracuse(1975).

[37] I. S. Shapiro, Phys.Rep. 35 (1978) 129.

[38] R. L. Jaffe, Phys.Rev. D17 (1978) 1444.

[39] C. B. Dover and J. M. Richard, Ann.Phys. 121 (1979) 70.

[40] F. Myhrer and A. W. Thomas, Phys.Lett. 64B (1976) 59.

[41] A. Zallo, private communication.

[42] R. Baldini, P. Gauzzi, S. Pacetti, E. Pasqualucci, Y. Srivastava, Eur.Phys.Jour. C11 (1999) 4.

[43] P. Stoler, Phys. Rev. D 44 (1991) 73.

[44] B. O. Kerbikov and A. E. Kudryavtsev, Nucl.Phys. A558, 177 (1993).

[45] A. Donnachie, H. Mirzaie, Z. Phys. **C33**(1987) 407.

[46] D. E. Groom et al., Eur. Phys. J. **C15** (2000) 1.

[47] E.V.Anashkin et al, ICFA Instr. Bull. v.5 (1988) 18.

[48] M.N.Achasov et al., Nucl.Instrum.Meth. A449 (2000) 125-139, hep-ex/9909015.

[49] S.Dolinsky et al., Phys.Rep. V.202, No.3, (1991) 138.

[50] A.Antonelli et al., Z.Phys. C56, (1992) 15.

[51] M.N.Achasov et al., Phys.Lett. B462 (1999) 365-370, hep-ex/9910001.

[52] L.M.Kurdadze et al, JETP Lett, 47, (1988), 512; 433, (1986), 643.

[53] D.Bisello et al., Preprint LAL 90-35, (1990).

[54] C.Bacci et al., Nucl. Phys. B184, (1981), 31.

[55] Donnachie et al., Zeitschrift Phys, C34, (1987), 257.

[56] R.R.Akhmetshin et al, Phys.Lett.. B466, (1999), 392, hep-ex/9904024.

[57] R.R.Akhmetshin et al, hep-ex/0009013.

[58] J.Buon et al, Phys.Lett.. 118B, (1982), 221.

[59] D.Bisello et al., Zeitschrift Phys, C39, (1988), 13., C52, (1991), 227.

[60] R. Landua, Ann. Rev. Nuc. Part. Phys. **46** (1996) 351-393.

[61] M. Diehl et al.,PRL **81**(1998) 1782.

[62] J. Gronberg et al., Phys. Rev. D **57** (1998) 33.

[63] M. Diehl, T. Gousset, B. Pire, hep-ph/0003233.

[64] V. G. Serbo, talk given at Photon 2000, 26-31 August 200 Ambleside U.K.(http:://photon2000.lancs.ac.uk/photon2000)

[65] L. Bartoszek et al., Nucl. Instr. and Meth. **A301**(1991)47.

[66] Hongguo Zhu, "A Measurement of the Neutron Electric Form Factor in $\vec{D}(\vec{e},e'n)p$ Quasi-elastic Scattering at $Q^2 = 0.5$ (GeV/c)^2", Ph.D Thesis, University of Virginia, August 2000, unpublished.

[67] F. M. Renard, Basics of Electron Positron Collisions, Editions Frontieres, Gif sur Yvette, France (1981).

[68] M. K. Jones et al., nucl-ex-9910005 (1999), submitted to Phys. Rev. Lett.

[69] X. C. Lou, W. M. Dunwoodie, BABAR BAD XX.

[70] F. Anulli, R. Baldini, A. Calcaterra, R. DeSangro, D. Falciai, A. Zallo, BABAR note 437.

[71] R. Baldini, R. DeSangro, A. Palano, A. Zallo, BABAR note 223; S. Bagnasco et al., BABAR BAD 56.